Tight junction ZO proteins maintain tissue fluidity, ensuring efficient collective cell migration

Mark Skamrahl, Hongtao Pang, Maximilian Ferle, Jannis Gottwald, Angela Rübeling, Riccardo Maraspini, Alf Honigmann, Tabea A. Oswald, and Andreas Janshoff**

M. Skamrahl, H. Pang, M. Ferle, J. Gottwald, Prof. Dr. A. Janshoff
University of Göttingen, Institute of Physical Chemistry,
Tammannstr. 6, 37077 Göttingen, Germany
E-mail: ajansho@gwdg.de

A. Rübeling, Dr. T. A. Oswald
University of Göttingen, Institute of Organic and Biomolecular Chemistry,
Tammannstr. 2, 37077 Göttingen, Germany
E-mail: toswald@gwdg.de

Dr. R. Maraspini, Dr. A. Honigmann
Max Planck Institute of Molecular Cell Biology and Genetics,
Pfotenhauerstraße 108, 01307 Dresden, Germany

Keywords: tight junctions, collective cell migration, jamming, cell mechanics, atomic force microscopy

Abstract

Tight junctions are pivotal components of epithelial tissues connecting neighboring cells to provide protective barriers. However, explicit knowledge of their role during other crucial biological processes, such as collective cell migration, remains sparse. Here, the importance of the tight junction proteins ZO1 and ZO2 for epithelial migration is investigated employing video microscopy in conjunction with velocimetry, segmentation, cell tracking, and atomic force microscopy/spectroscopy. The results indicate that ZO proteins are necessary for fast and coherent migration. In particular, ZO1 and 2 loss induces actomyosin remodeling away from the central cortex towards the periphery of individual cells, resulting in altered viscoelastic properties. A tug-of-war emerges between two cell populations with distinct morphological and mechanical properties: 1) smaller and highly contractile cells with an outwards bulged apical membrane, and 2) larger, flattened cells, which, due to tensile stress, display a higher proliferation rate. In response, the cell density increases, leading to crowding-induced jamming and more small cells over time. These smaller cells are particularly immobile and therefore drive jamming. Knockout of only ZO1 induces a similar but less pronounced behavior. This study shows that ZO proteins are necessary for efficient collective cell migration by maintaining tissue fluidity and controlling proliferation.

1. Introduction

Cellular junctions endow epithelial tissues with their barrier functions by physically connecting neighboring cells. Junction integrity is critical to prevent many diseases. While, among the various junction types, adherens junctions are typically considered as mechanical couplers between cells in epithelia, recent evidence also suggests an important mechanical role for tight junctions (TJs).[1–7] It is conceived that TJs provide a mechanical feedback system regulating the contractility of individual cells via the actomyosin cytoskeleton and their adhesion strength to neighboring cells.[1,4,8–11] Specifically, it was shown that TJs provide a negative mechanical feedback to individual cells in a layer, so that they contract less, lowering the forces on the adherens junctions.[1,4] Once TJ formation is inhibited, cells respond by building thick actomyosin rings at the cell periphery, which, upon contraction, lead to severe heterogeneity of the cell morphology, particularly visible at the apical side.[8,4,12,11] Since this mechanical TJ-based mechanism was established only recently, explicit knowledge of its implications for crucial biological processes such as collective migration remains limited. Collective cell migration depends on an intricate interplay of the mechanical interaction in a cell layer ranging from single cells, e.g., leader cells at the advancing migration front, to the collective behavior of the cell sheet on a mesoscopic level.[13–18] This interplay depends on the fine tuning of cell motility, density, contractility, and cell-cell adhesion.[19–31]

Important advances have been achieved in understanding how collective cell migration is generally influenced by the adhesion-mediating junction proteins.[27] However, there is controversial evidence on the influence of different TJ components on collective migration. While knockout of the transmembrane protein occludin has been shown to severely compromise migration dynamics,[32] interference with the scaffolding ZO (zonula occludens) proteins was associated with both migration acceleration (ZO2; Raya-Sandino et al.[33], ZO1;

Bazellières et al.[27]) as well as deceleration (ZO1; Tornavaca et al.[5], ZO3; Bazellières et al.[27]) in different epithelial cell lines. This discrepancy in evidence might be explained by the fact that such studies focused on the modification of only one single TJ component at a time. More recently, there were in-depth efforts to understand the impact of interfering with multiple ZO proteins on cell- and mechanobiology in general.[1,2,4] However, the consequences for collective cell migration remain elusive.

To close this gap in knowledge, we performed migration experiments with ZO1 KO (single knockout) as well as ZO1/2 dKD (double knockdown) MDCK II cell lines in combination with mechanical measurements and various imaging techniques. We showed that ZO protein loss severely diminishes migration speed and coherence. This was induced by cellular jamming, or liquid-to-solid-like transition, upon progressing migration due to uncontrolled proliferation, concomitant with actomyosin remodeling leading to pronounced changes of cellular mechanics. In particular, a coexistence of elevated small cells with strong actin rings at the periphery and large flat ones was one of the hallmarks explaining the altered collective migration. The enhanced proliferation is predominately observed for flat and strained cells originating most likely from tensile forces generated by the smaller but highly contractile cells and exerted on the adjacent larger cells. The increase in proliferation leads to jamming and eventually limits migration speed and reduces order parameters associated with collective migration.

ZO1 KO cells showed similar but less pronounced proliferational, mechanical, and cytoskeletal adaptations. Albeit they also exhibited signs of jamming at late migration stages, no distinct small and large cell phenotypes arose as found for dKD cells. This finding emphasizes that the coexistence of large cells, which proliferate more and induce crowding, and small cells, which migrate less actively, is an important feature of jamming in TJ-deficient cells.

2. Results

2.1. ZO proteins ensure fast and coherent epithelial migration

To investigate the role of TJs in collective migration, we first performed migration experiments using phase contrast microscopy combined with particle image velocimetry (PIV)-based analyses (**Figure 1**A/B).[34] Strikingly, video microscopy revealed that migration velocity of dKD cells was substantially lower than that of WT (wildtype) cells and even ZO1 KO cells. We first summarized data from the overall migration dynamics of the whole cell layers by averaging over all time points and all vectors (Figure 1C). While ZO1 KO cells did not display significant changes in migration dynamics (16 ± 2 µm h^{-1} (mean ± s.d.)) compared with WT MDCK II (18 ± 2 µm h^{-1} (mean ± s.d.), $p = 0.13$), ZO1/2 dKD cells migrated significantly slower (8 ± 1 µm h^{-1} (mean ± s.d.), $p < 0.001$). Additionally, we calculated the order parameter, which quantifies how directed the local motion is towards the migration edge (Figure 1C). We found that dKD cells migrated less directed (order parameter of 0.12 ± 0.04) than WT (0.29 ± 0.09) and ZO1 KO (0.31 ± 0.08) cells ($p < 0.001$), respectively.

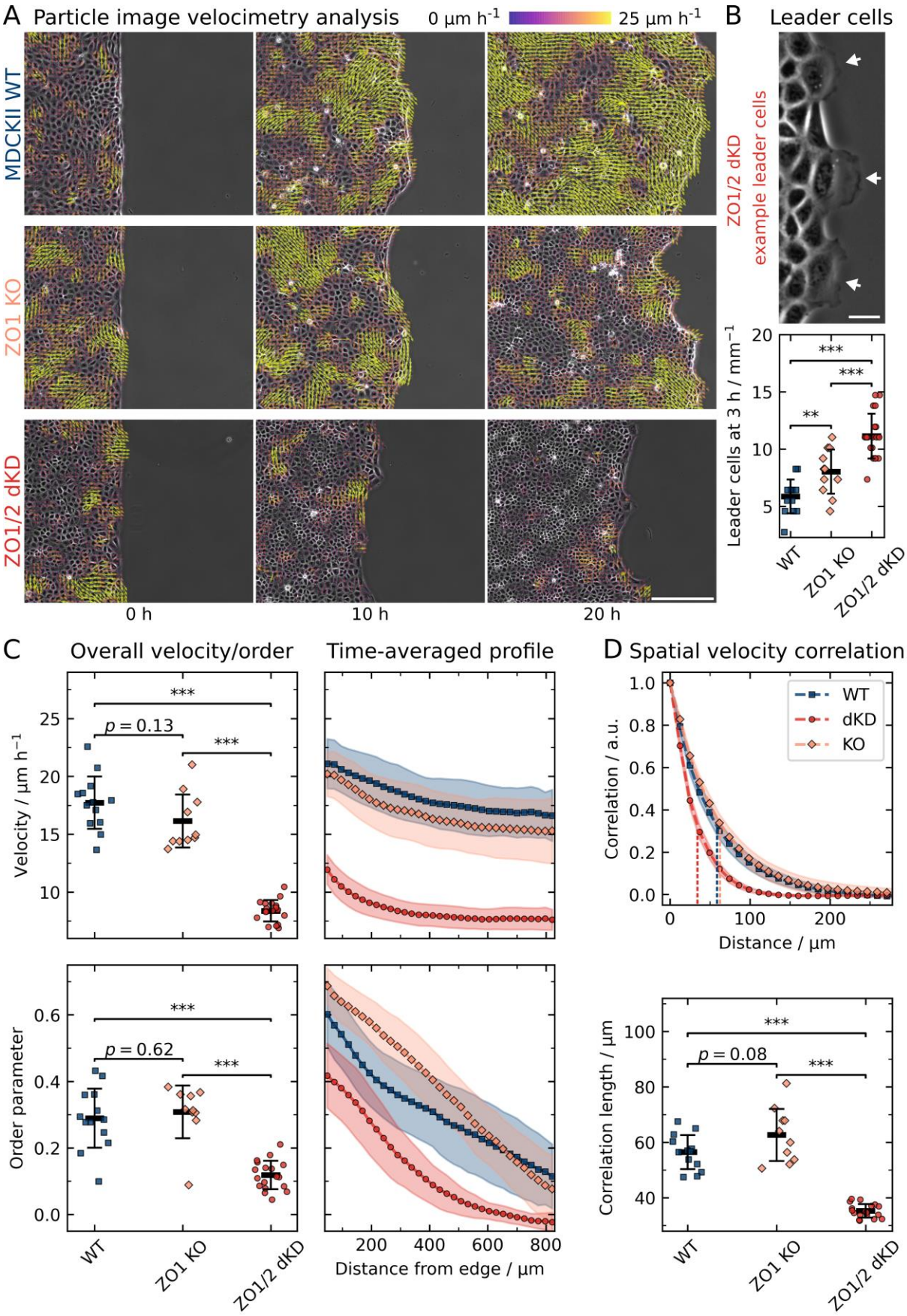

110 **Figure 1.** Collective cell migration dynamics of wild type (WT), ZO1 knockout (KO) and

111 ZO1/2 double knockdown (dKD) MDCK II cells. A) Migrating cell monolayers with the

corresponding velocity vectors obtained from particle image velocimetry (PIV). To enhance the figure's visibility, cropped images are shown (about a fourth of the original field of view). Scale bar: 200 µm. B) Quantification of leader cell emergence and a corresponding dKD example. The amount of leader cells was normalized by the respective migration edge length for better comparison. Scale bar: 25 µm. C) The overall velocity and order are defined as the average over all vectors and time points, velocity and order were additionally averaged over time along the distance from the edge of the cell layer. D) Spatial velocity function. Vertical dashed lines indicate the corresponding characteristic correlation lengths below. All data are shown as means and standard deviations. Sample sizes (independent experiments): 13 (WT), 10 (KO), 18 (dKD).

To characterize the velocity transmission from the migration edge into the bulk of the monolayer, time-averaged velocity and order profiles were computed (Figure 1C). Here, we observed a subtle velocity decay in the range of the standard deviation with increasing distance from the migration edge for the WT and the ZO1 KO cells from about 20 µm h^{-1} at the edge to 17 µm h^{-1} (15% decrease) 400 µm away from the edge, while the dKD cells showed a sharper velocity drop from approximately 12 µm h^{-1} to 8 µm h^{-1} (33% decrease), approaching a plateau at about 400 µm, indicating an impaired velocity transmission from the edge into the layer. The order parameter decreased with increasing distance from the edge into the bulk layer for all three cell lines. Interestingly, for dKD cells the order parameter was not only lower at every distance from the edge but even approached zero at approximately 600 µm (indicating zero net movement towards the edge). This highlights that the cell collectivity was diminished, which goes hand in hand with the increased number of leader cells emerging from the dKD layers (Figure 1B). Almost twice as many leader cells were observed in the dKD (11 ± 2 mm^{-1} (mean ± s.d.)) as in the WT monolayers (6 ± 2 mm^{-1} (mean ± s.d.), $p < 0.001$). The ZO1 KO cells also showed an elevated number of leader cells

(8 ± 2 mm^{-1} (mean ± s.d.), $p < 0.01$) compared with the WT, albeit less leader cells than the dKD variant.

To further study the reach of force transmission, we also computed the spatial velocity correlation of the migrating cells (Figure 1D). While the spatial velocity correlation of ZO1 KO cells decayed slightly slower than that of WT cells, yielding longer correlations lengths of 63 ± 9 µm (mean ± s.d.) for the KO than 57 ± 6 µm (mean ± s.d.) for the WT ($p = 0.08$), dKD cells showed considerably shorter correlation lengths of 35 ± 2 µm (mean ± s.d.) than both WT and ZO1 KO cells ($p < 0.001$, respectively).

Taken together, these findings suggest that ZO1/2 dKD cells migrate slower, less correlated, and less directed than the WT, thereby showing a significant loss of the hallmark parameters of cell collectivity. This behavior could be induced by a variety of mechanisms, from biochemical signaling to cell mechanical adaptations and possibly cellular jamming, in which the last two ones will be investigated further (*vide infra*).

2.2 ZO proteins prevent jamming and cell crowding

Already from visual inspection of the epithelia, it was obvious that the KO and particularly the dKD monolayers became increasingly dense over time during migration due to continuous proliferation, whereas the WT layers showed no obvious change in density. Therefore, we quantified this peculiarity and also examined the impact of crowding on collective migration. While PIV is a well-established technique for the quantification of migration dynamics of cell collectives, it lacks information about the behavior of individual cells in the layer. To overcome this limitation, we applied the automated cell segmentation algorithm Cellpose (Stringer et al.) outlining the area occupied by each individual cell in 2D as shown in **Figure 2**A.[35]

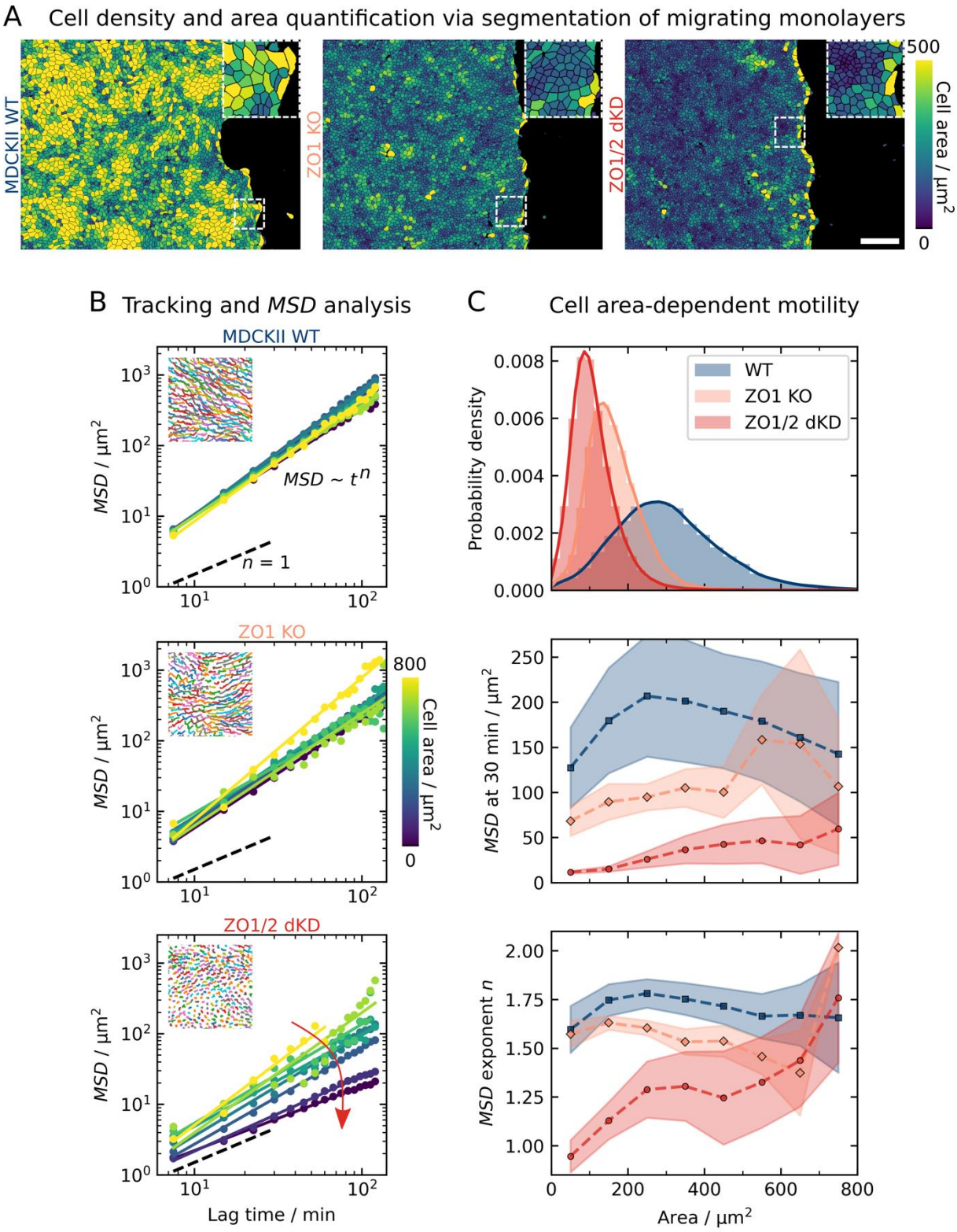

163 **Figure 2.** Cell area-dependent motility analysis based on segmentation and tracking, revealing
164 crowding-induced jamming of ZO depleted cells during late-stage migration. A) Segmented
165 cells in migrating monolayers after 20 h of migration, colored by the respective individual
166 projected area in 2D. Scale bar: 200 µm. B) Tracking and mean-square-displacement (*MSD*)

167 analysis. *MSD*s and corresponding power law regression for a time window between 19 h and
168 21 h are shown for cells in 100 µm^2 area bins. The insets show exemplary tracks colored
169 randomly. The red arrow indicates a decrease of the *MSD* with decreasing area, only
170 prominent for the dKD cells. C) Cell area-dependent *MSD* parameters from B. The area
171 distribution of all cells after 20 h of migration is shown at the top. ZO protein interference
172 induced a shift to smaller areas with a pronounced skewness of 1.23 for the KO and 2.25 for
173 the dKD as compared with the WT cells (0.94). Below, the *MSD* at 30 min and the power law
174 exponent *n* are plotted vs the cell area. Points correspond to bins of 100 µm^2 (around the point
175 location), starting from 0 µm^2. Means and standard deviations are shown. Sample sizes
176 (independent experiments): 13 (WT), 9 (KO), 18 (dKD).
177
178 Indeed, we were able to quantify a severe lack of contact inhibition of proliferation for the
179 dKD cells as indicated by a strong increase of the cell density over time during migration
180 (Figure S1A), indicating a possible jamming mechanism that conceivably compromised
181 migration dynamics and cooperativity. While the density of the WT cells remained
182 approximately constant, the KO cells displayed a cellular density increase similar to dKD
183 cells but not as pronounced. Yet, this density increase could also come from a lack of edge
184 displacement combined with additional cells moving into the field of view. To confirm that
185 mainly proliferation induced the density increase, we quantified cell density without a
186 migration edge in a separate experiment (Figure S1D). Indeed, the dKD cell density increased
187 stronger within the first 60 h and then reached a higher steady-state density than either WT or
188 KO cells.
189 Two prominent parameters can be employed to characterize jamming transitions of cell
190 layers: cell density and cell shape. Particle-based models attribute jamming to an increased
191 cell density,[36] whereas vertex models predict the shape of cells, as quantified by the shape
192 index or the projected aspect ratio in 2D, to be the main determinant for jamming.[23]

However, along with the density increase with elapsed time, we did not observe a clear change in the projected cell aspect ratio in 2D (length divided by width) as shown in Figure S1A. Except for a short increase to a median aspect ratio of 1.60 around 5 h for the WT, all cell lines had a similar and only very subtly decreasing aspect ratio at around 1.45. However, the WT cells exhibited a slightly higher aspect ratio at all times, with a slightly broader distribution shifted to larger values (Figure S1B). Note that the observed aspect ratio values here are above the jamming threshold of 1.18,[20] as calculated from the shape index of 3.81 as previously proposed by Bi et al.[23] Notably, there was no correlated variation between cell area and aspect ratio of individual cells (Figure S1C), rendering these parameters largely independent of each other for each cell.

The decrease of migration velocity over time of dKD cells together with their increased proliferation indicate jamming as a pivotal determinant of these cells. A marked difference in the averaged PIV data of WT and ZO1-KO became apparent only after 15 h, when the KO also slowed down and showed uncontrolled proliferation and slightly decreasing aspect ratios, similar to the behavior of dKD cells. However, the dKD cells display the slowest dynamics of all three cell lines, which could not be attributed solely to a change in the cell density, as this was also altered in ZO1-KO cells.

So far, our purely mesoscopic approach reveals a morphological heterogeneity (small and large cells) particularly for dKD cells at later time points (Figure 2A). This brought up the question, whether these morphological differences could be responsible for the impaired cellular dynamics. Therefore, we utilized single cell tracking to investigate the dynamics of individual cells in a layer during late-stage migration (19-21 h after insert removal), depending on the cell density and the projected cell area in 2D. We found that the motility, as quantified by the *MSD* (mean square displacement), of WT and KO cells generally did not depend on the cell area. In contrast, the *MSDs* of individual dKD cells show a clear dependency on cell area (Figure 2B). Specifically, we observed that the movement amplitude

(*MSD* at 30 min) as well as the exponent *n* of the *MSD*s as a function of lag time rises with increasing cell area for the dKD. The small and most abundant bulk cells with an area around the distribution peak of about 120 µm^2 showed passive diffusion-like movement with $n \sim 1$ and small amplitudes of about 10 µm^2. In contrast, the larger cells exhibited active motion with up to $n = 1.75$, which is similar to the WT cells and close to straight-line motion at $n = 1.75$, and five-fold increased amplitudes of 50 µm^2 (Figure 2C). The KO cells had a similarly skewed cell area distribution with small bulk cell of about 180 µm^2 showing movement amplitudes of about 80 µm^2 while the sparse large cells moved about 110-200 µm^2. However, neither WT nor KO cells showed any clear dependence of *n* on the cell area. Interestingly, the WT showed a more symmetrical cell-area distribution around 280 µm^2 (skewness of 0.94 as compared with 1.23 for the KO and 2.25 for the dKD cells) with averaged-sized cells showing the largest movements (*MSD* around 200 µm^2) and cells at the extreme ends of the distribution moving less (*MSD* of about 130 µm^2). Importantly, we did not find any clear dependence of the individual cell motility on the aspect ratio (Figure S1B). Together, these results show that cell density is the determining factor explaining the observed jamming of dKD cells due to an abundance of slow-moving small cells coexisting with faster-moving large and actively dividing cells.

As we have identified an important connection between jamming, proliferation, and migration speed in cells lacking ZO proteins, we aimed to reverse the cellular crowding and jamming by the inhibition of proliferation using the well-established drug Mitomycin C.[19,21,37–39] As expected, upon Mitomycin C treatment, the density of all three cell lines did not increase but instead even slightly decreased over time, confirming a successful inhibition of proliferation (Figure S2A). Concomitantly, the migration velocity increased while the overall aspect ratio slightly decreased over time. To quantify the impact of proliferation inhibition, we now focused on the late-stage migration dynamics after 19 h (**Figure 3**A).

244 The drug increased the migration speed of WT MDCK II cells from 19 ± 6 μm h^{-1} to

245 29 ± 2 μm h^{-1} (mean ± s.d., $p < 0.001$), whereas the order parameter and correlation length did

246 not change significantly ($p = 0.15$ and $p = 0.26$, respectively).

247

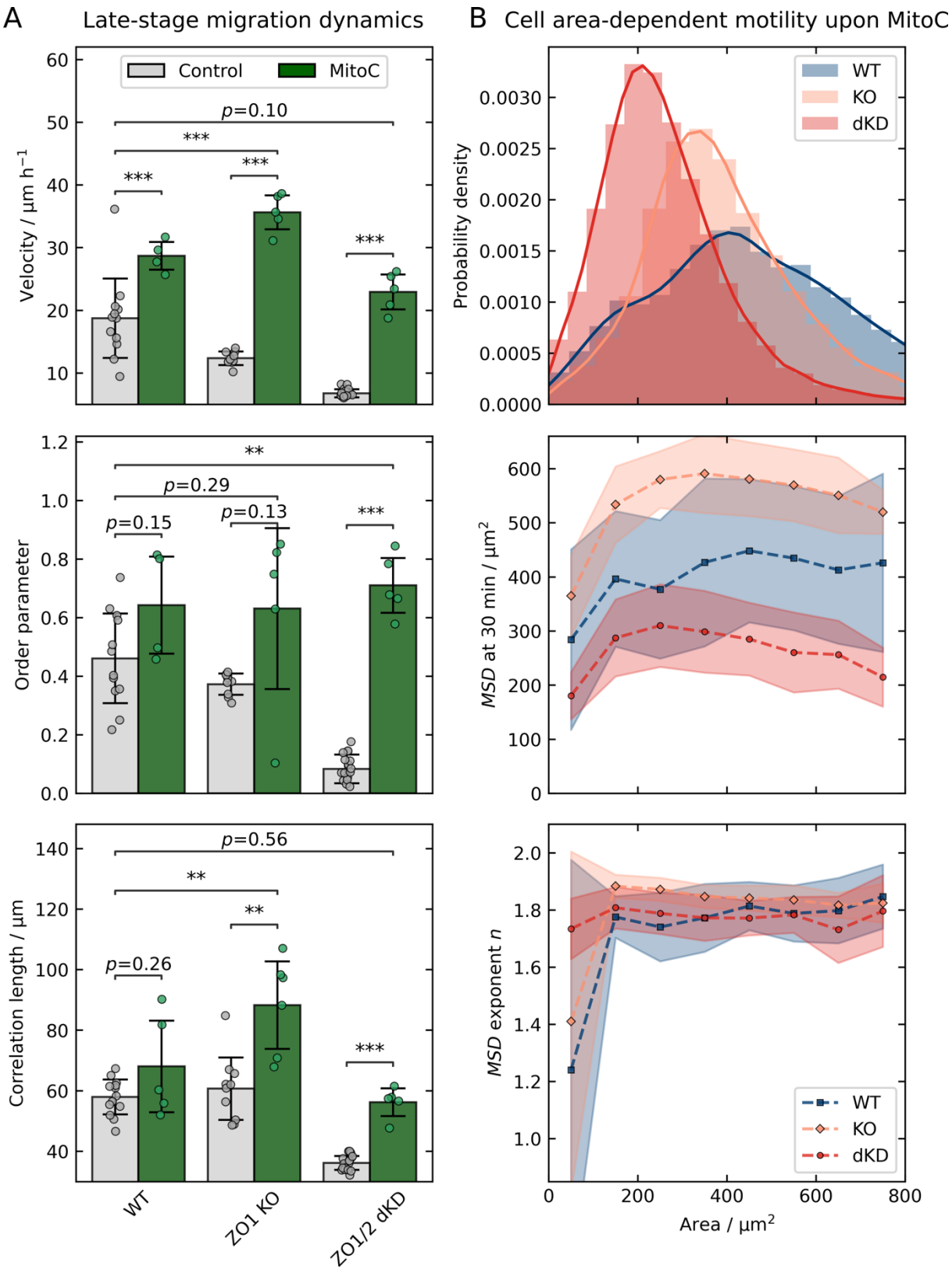

248 **Figure 3.** Late-stage collective migration dynamics enhanced by proliferation inhibition with
249 Mitomycin C (MitoC). A) Migration dynamics after 19 h with (control) and without
250 proliferation (MitoC). Overall velocity, order and correlation were calculated as in Figure 1.
251 B) Cell area-dependent *MSD* parameters upon proliferation inhibition (MitoC treatment). The

252 area distribution of all MitoC-treated cells at 20 h of migration is shown at the top. Larger cell
253 areas and skewness parameters of 1.01 (WT), 1.36 (KO), and 1.83 (dKD) were observed.
254 Below, the *MSD* at 30 min and the power law exponent *n* are plotted vs the cell area. *MSD*s
255 and corresponding power law fits were calculated for a time window between 19 h and 21 h,
256 in accordance with Figure 2. Points correspond to bins of 100 μm^2 (around the point location),
257 starting from 0 μm^2. Means and standard deviations are shown.
258
259 In contrast, we observed a significant increase of all migration parameters for the dKD cells
260 (Figure 3A) explaining the observed boost in dynamics. Specifically, the dKD velocity
261 increased from 7 ± 1 μm h^{-1} to 23 ± 3 μm h^{-1} (mean ± s.d., $p < 0.001$), which is even slightly
262 higher than the velocity of untreated WT cells ($p = 0.10$), the order increased from
263 0.08 ± 0.05 to 0.7 ± 0.1 (mean ± s.d., $p < 0.001$), which is significantly higher than that of
264 untreated WT cells (0.5 ± 0.2 (mean ± s.d., $p < 0.01$)), and the correlation length increased
265 from 36 ± 2 μm to 56 ± 5 μm (mean ± s.d., $p < 0.001$), which is similar to the correlation
266 length of untreated WT cells, being 58 ± 6 μm (mean ± s.d., $p = 0.56$).
267 The ZO 1 KO cells showed a similar behavior as the dKD cells upon proliferation inhibition,
268 but with a less pronounced increase in all parameters. The velocity of KO cells increased in
269 the presence of Mitomycin C from 12 ± 1 μm h^{-1} to 35 ± 3 μm h^{-1} (mean ± s.d., $p < 0.001$),
270 which is also significantly higher than the velocity of untreated WT cells ($p < 0.001$), the
271 order parameter increased from 0.37 ± 0.04 to 0.6 ± 0.3 (mean ± s.d., $p = 0.13$), which is
272 slightly higher than the order parameter of untreated WT cells ($p = 0.29$), and the correlation
273 length increased from 61 ± 10 μm to 88 ± 14 μm (mean ± s.d., $p < 0.01$), which is also higher
274 than the correlation length of untreated WT cells ($p < 0.01$).
275 Taken together, the velocimetry data clearly showed that inhibition of proliferation largely
276 reversed the jamming process of dKD, and, less pronounced, that of ZO1 KO cells, by
277 preventing an uncontrolled density increase.

Interestingly, the area-dependence of the *MSD* of dKD cells during late migration (19-21 h, *vide supra*) also vanished upon inhibition of proliferation (Figure 3B). In general, the individual cell area was larger in the presence Mitomycin C for all three cell lines as expected for proliferation inhibition. This was most pronounced for dKD cells, where the cell area increased from 120 μm^2 to about 220 μm^2 (see area distribution in Figure 3B). The *MSD* also showed a higher amplitude (*MSD* at 30 min) as well as exponent *n* for all treated cell lines than for untreated cells. Specifically, the dKD *MSD* amplitude was between 200 μm^2 and 300 μm^2 upon proliferation inhibition, which is slightly higher than for the untreated WT cells (150-200 μm^2). The treated WT cells showed slightly larger amplitudes of 300-400 μm^2 and the KO cells surpassed both other cell lines at about 300-550 μm^2. Interestingly, the *MSD* exponent is equalized upon proliferation inhibition for all cell lines at about 1.8, which indicates completely restored directionality. This is in good accordance with the higher order parameter upon proliferation inhibition as shown in Figure 3A (*vide supra*).

Notably, upon proliferation inhibition we did not observe a clear trend in the movement amplitude and the *MSD* exponent with decreasing cell area as before anymore (Figure 3B). In contrast to untreated KO and dKD cells, upon inhibited proliferation the KO and dKD bulk cells of about 380 μm^2 and 220 μm^2, respectively, even showed a slight peak in the movement amplitude while larger and smaller cells both moved slightly less. The *MSD* exponent remained constant with varying area.

Together, these results indicate that the strong crowding-induced jamming could be reversed by the inhibition of proliferation. However, it is important to note that, besides proliferation, Mitomycin C might also influence other cellular functions, which could potentially contribute to the observed migration dynamics.

2.3 Successful ZO knockdown induces actomyosin remodeling

Given such severe phenotypical changes in the migration dynamics and proliferation rates of the ZO1 KO and dKD cells, we sought to investigate the phenomena also on the molecular level.

First, to ensure successful genetic knockout, we performed confocal immunofluorescence microscopy. Indeed, ZO1 and ZO2 proteins were no longer visible upon double knockdown (Figure S3). Corresponding western blot analyses can be found in Beutel et al.[40]

ZO1 knockout was also successful as shown in Figure S3A. Importantly, ZO2 was only slightly upregulated indicating a possible compensation for ZO1. Notably, adherens junctions are not obviously affected (Figure S4) highlighting that the observations described here mainly reflect the ZO protein loss.

Since the transmembrane proteins in tight junctions are connected to the actin cytoskeleton via ZO proteins, we next investigated changes in the actomyosin architecture of the cells (**Figure 4**). Indeed, the actin cytoskeleton of the dKD cells was changed in a distinct way as shown in Figure 4C. Actin was accumulated at the periphery of individual cells, organized in thick rings, which were slightly separated at the apical plane of neighboring cells. ZO1 knockout cells on the other hand showed an intermediate phenotype with a less marked actin accumulation at cell-cell borders with a slight separation into two thinner cables. In comparison, the WT cells displayed the typical actin structure of MDCK II cells with a continuous mesh between cells and without any separation between neighboring cells or any obvious actin accumulation.

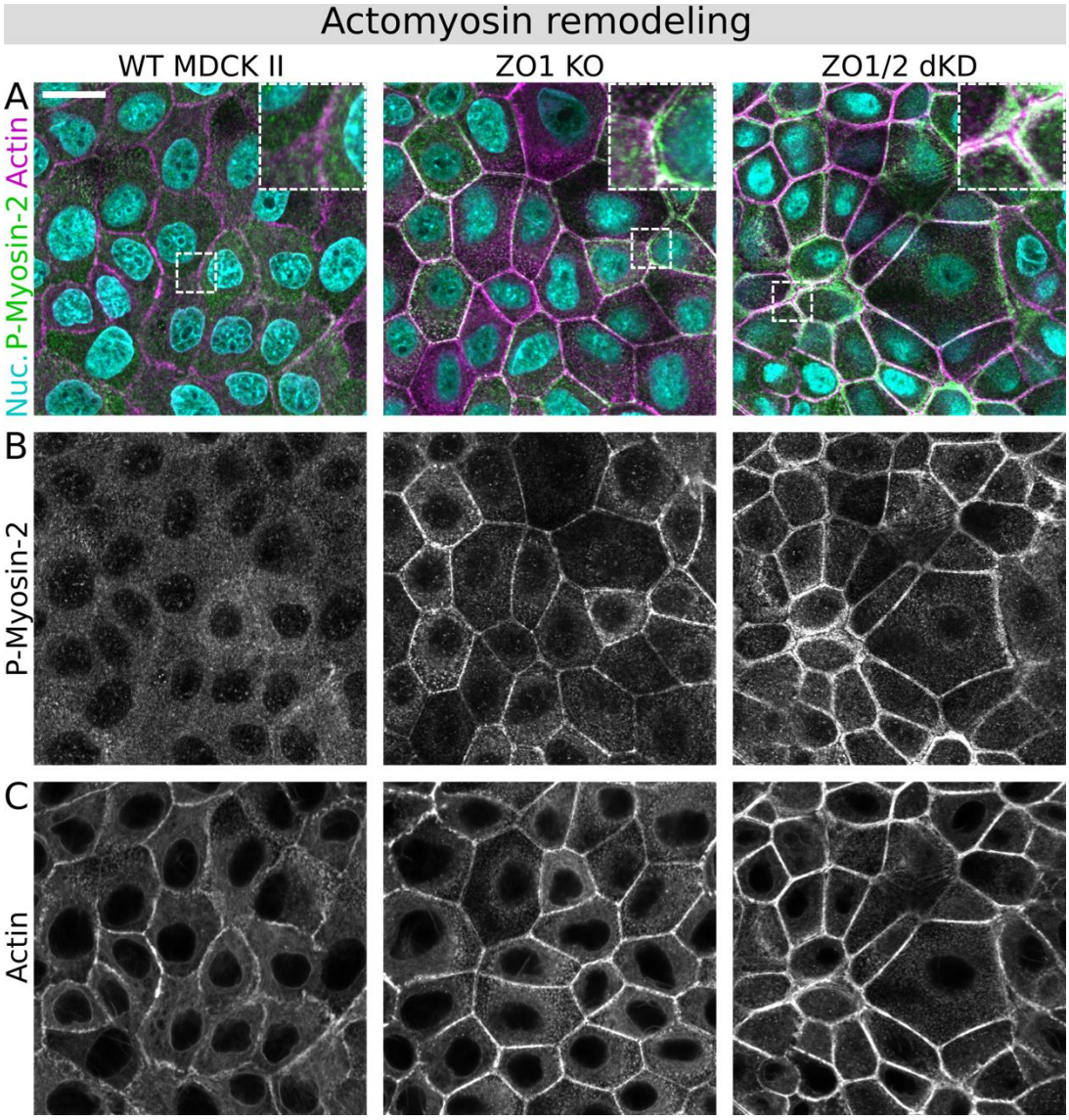

326 **Figure 4.** Actomyosin architecture remodeling upon ZO protein interference. A)
327 Phosphorylated Myosin-2 (P-Myosin-2; green), actin (magenta) and nuclei co-staining of all
328 three MDCK II cell lines. B) Corresponding gray-scale images of P-Myosin-2. C)
329 Corresponding gray-scale images of actin. Scale bar: 20 µm.
330
331 In addition, activated (phospho-) myosin-2 upregulation was particularly prominent at the
332 cell-cell border in conjunction with the actin accumulation in dKD cells (Figure 4B),
333 indicating upregulated actomyosin contractility. Interestingly, it seems that smaller dKD cells
334 accumulated more peripheral actomyosin than their larger neighbors. On the other hand, ZO1
335 KO also showed accumulation of activated myosin at the cell periphery, albeit not as severe

as in the dKD. In contrast, the WT cells showed little activated myosin without any prominent pattern or structure. Additionally, the occurrence of many small and some large dKD cells (as described above) was observed. In contrast, the WT and KO cell area appeared much more homogeneous.

Taken together, these findings show that interfering with ZO proteins induces actin remodeling accompanied by myosin activation and accumulation, suggesting possible cell mechanical and morphological changes.

2.4 The cell topography reflects actomyosin remodeling upon ZO knockdown and shows a heterogeneous apical cell height distribution

Because severe actomyosin remodeling and accumulation at the apical cell periphery was observed, we also expected changes in the cellular topography (**Figure 5**). Consistent with the changes in the actomyosin structures, using AFM (atomic force microscopy) imaging we found prominently elevated ring-like structures at the periphery of individual dKD cells, slightly separated from each other (zoom-in in Figure 5A). In contrast, wild type cells exhibit a less pronounced but continuous cell border. ZO1 KO cells showed only a slight change of the cell border topography.

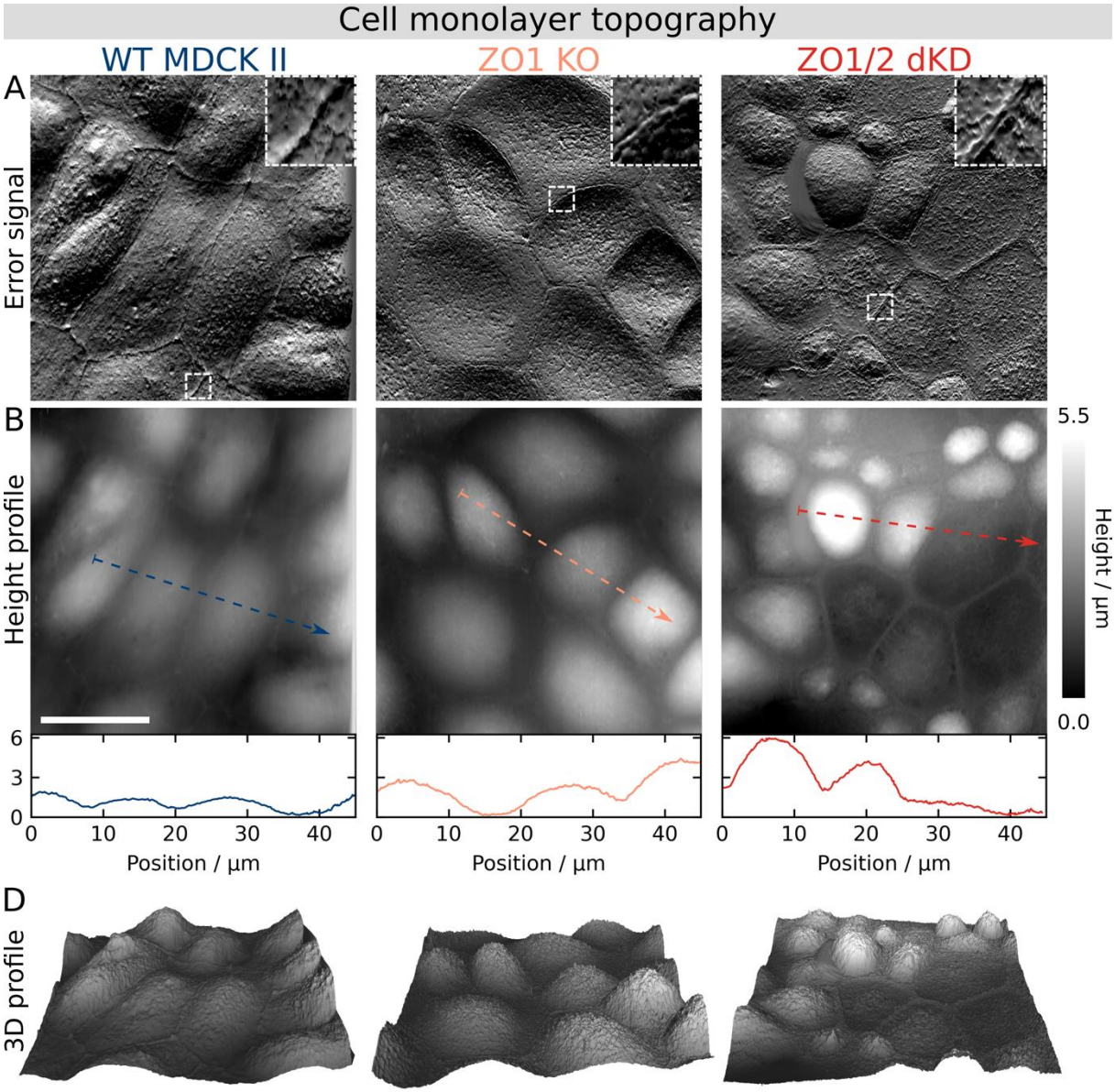

354 **Figure 5.** Cell monolayer topography adaptations reflect the actomyosin remodeling upon ZO
355 protein interference as shown by AFM imaging. A) Error signal (deflection images). B)
356 Height profile and cross-sections. D) Corresponding 3D topography maps, slightly up-scaled
357 vertically, with the *z*-axis length being 20% of the *x*/*y*-axis (13.3% corresponds to an aspect
358 ratio of 1). Scale bar: 20 µm.

359

360 Furthermore, AFM imaging confirmed the data from confocal fluorescence microscopy and
361 segmentation indicating a pronounced height and area heterogeneity in dKD cells. While the
362 apical cap of cells with a small area of about 100 µm^2 (compare with chapter 2.2) was several

363 micrometers high (> 3 µm), other cells were larger in area but do not exhibit any distinct
364 apical cap rising above the peripheral ring. In comparison, the apical cap of WT cells was
365 typically 1-1.5 µm high and homogenously distributed across the monolayer. The ZO1 KO
366 cells displayed an intermediate phenotype with a homogenous cap height distribution, which
367 are typically slightly higher than WT cells, at about 2-3 µm.
368 In conjunction with the actomyosin results, these data show that ZO1/2 dKD consistently
369 induces distinct molecular and topographical changes, most notably, severe actomyosin
370 accumulation underneath the membrane at the cell-cell borders in the small cell population
371 being responsible for altered mechanical properties, which are scrutinized in the next chapter.
372

373 **2.5 ZO proteins are necessary for mechanical integrity and tissue fluidity**

374 In light of the prominent cell topography adaptations and concomitant actomyosin
375 remodeling, and because contact inhibition of proliferation and jamming are typically tightly
376 coupled with cellular mechanics, the consequences of ZO depletion for cell mechanics were
377 investigated. To this end, we performed AFM measurements with an emphasis on force
378 relaxation experiments that also permit to assess the rheological properties of the cells. First,
379 force volume imaging showed that stiffness was increased considerably at the cell periphery
380 of ZO1 KO and dKD compared with WT cells (AFM maps in **Figure 6**A), whereas the center
381 appeared to be softer compared with WT cells.
382

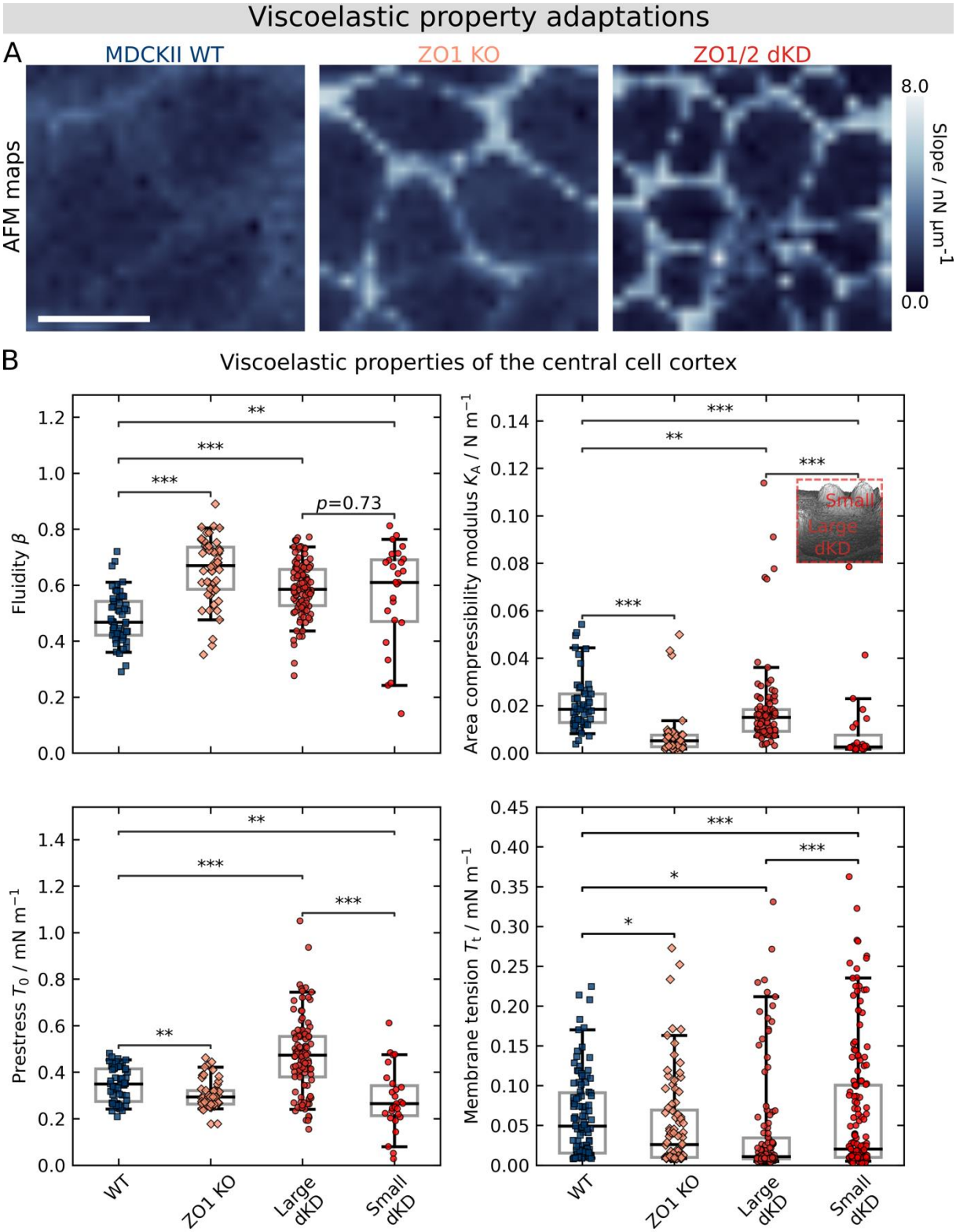

Figure 6. ZO proteins ensure viscoelastic integrity of cells as shown by AFM (atomic force microscopy). A) Exemplary AFM maps of migrating WT, ZO1 KO and ZO1/2 dKD cells showing the slope of the force during contact, mirroring the apparent stiffness of cells. Scale bar: 20 µm. B) Site-specific viscoelastic properties of the central cell cortex. Fluidity β, area

compressibility modulus K_A, prestress T_0, and membrane tension T_t are shown. Five curves were immediately recorded on the same position at the center of one cell. Individual data points represent the average of the respective fitting parameter for an individual cell. The boxes show the median and the upper and lower quartiles. Whiskers indicate the 5^{th} and 95^{th} percentile.

This is consistent with the observed accumulation of actin into a contractile actomyosin ring and the altered topography at the cell periphery of ZO depleted cells. Apart from stiffness maps, we also used site-specific indentation experiments followed by force relaxation to study the mechanical and rheological cortex properties in greater detail. The model we applied was introduced recently by Cordes et al.[41] Briefly, it considers stress relaxation of the cortex according to a power law providing us with a prestress corresponding to the isotropic cortical tension T_0 plus membrane tension T_t, the area compressibility modulus K_A of the cortex and the fluidity β, which classifies the flowing propensity of the network. A β value of 1 corresponds to a Newtonian fluid whereas a value of 0 describes a solid. Since we observed a prominent heterogeneity of the dKD cell morphology with a flat surface observed for large cells and a high apical cap seen for smaller cells, we considered the resulting geometrical differences in the model and distinguished between large (about 200 μm^2) and small dKD cells (80 μm^2).

Notably, we observed statistically significant changes in all mechanical parameters upon ZO protein loss (Figure 6B).

Cortex-dominated prestress T_0 was significantly lower in the center of KO (0.30 ± 0.06 (median ± s.d.) mN m^{-1}, $p < 0.01$) and small dKD cells (0.27 ± 0.13 (median ± s.d.) mN m^{-1}, $p < 0.01$) than in the center of WT cells (0.35 ± 0.07 (median ± s.d.) mN m^{-1}), indicating a downregulation of the actin cortex in both populations due to remodeling of the actin cytoskeleton. In contrast, the large dKD cells showed an increased prestress (0.47 ± 0.16 (median ± s.d.) mN m^{-1}, $p < 0.001$ compared with WT as well as with small dKD

cells). This goes hand in hand with a flatter morphology indicative of area expansion, leading to higher tension - Generally, the prestress T_0 contains contributions from i) membrane tension that originates from adhesion of the plasma membrane to the underlying cytoskeleton, ii) area expansion of the apical shell and iii) active contraction by myosin II motors. To tell apart the contribution of the actin cortex from that of the plasma membrane-cytoskeleton attachment to the prestress T_0 we additionally pulled out membrane tethers upon retraction to measure the membrane tension T_t. We observed that T_t decreased upon ZO protein KO for all cell lines. It dropped from 0.05 ± 0.05 (median ± s.d.) mN m^{-1} (WT) to 0.03 ± 0.06 (median ± s.d.) mN m^{-1} (KO, $p < 0.05$), 0.01 ± 0.09 (median ± s.d.) mN m^{-1} (large dKD, $p < 0.001$), and to 0.02 ± 0.08 (median ± s.d.) mN m^{-1} (small dKD, $p < 0.05$). This shows that the prestress changes were only partly explainable by a decrease in membrane tension. However, the membrane tension of large dKD cells decreased, supporting the idea that prestress of the larger and flatter dKD cells stems from area expansion rather than a reinforced attachment of the cortex to the membrane.

Along with smaller prestress, we also observed a fluidization of the cortex represented by an increase of β from 0.5 ± 0.1 (median ± s.d.) to β = 0.7 ± 0.1 (median ± s.d., $p < 0.001$) for KO cells, and to β = 0.6 ± 0.2 (median ± s.d., $p < 0.01$) for the small dKD cells, respectively. Also, for large dKD cells an increase in fluidity was found (β = 0.6 ± 0.1 (median ± s.d.), $p < 0.001$). Recently we showed that fluidity and area compressibility modulus of the cortex are not necessarily independent parameters. Accordingly, the area compressibility modulus K_A decreased from 0.02 ± 0.01 (median ± s.d.) mN m^{-1} for WT to 0.005 ± 0.001 (median ± s.d.) mN m^{-1} for KO ($p < 0.001$) and to even 0.003 ± 0.002 (median ± s.d.) mN m^{-1} for small dKD cells ($p < 0.001$), respectively. For the large dKD cells, K_A fell by only 50% to 0.01 ± 0.01 (median ± s.d.) mN m^{-1} ($p < 0.01$) albeit the fluidity was rather high (β = 0.6 ± 0.1). Notably, the large dKD cells show a significantly higher K_A than the small dKD cells. This might indicate the presence of a prestressed cortex

with less membrane reservoir to compensate for the external deformation. This view is backed up by the finding that the geometrical apical membrane of the large dKD cells is also larger than that of the small dKD cells despite the apical bulging (as inferred from geometrical considerations based on the topography measurements in Figure 5). Interestingly, the large and prestressed dKD cells were observed to proliferate over twice as much as the small dKD cells (Figure S5), indicating a possible connection between the mechanical phenotype of the large dKD cells and proliferation.

The drop in area compressibility modulus in the small dKD and KO cells could be either due to a higher cortical elasticity or a larger apical excess area, giving rise to apparent area compressibility modules. Considering the substantial morphological changes of the apical membrane/cortex in response to ZO1/2 knock down, such as bulging of the cortex and the reported occurrence of membrane reservoirs (small dKD cells), it is conceivable that both effects contribute to the observed softening.

Taken together, these findings show a mechanical integrity loss upon ZO protein knockout: Actomyosin is recruited from the cortex to the periphery of individual cells building up a stiff and contractile actomyosin ring while leaving the apical cortex weakened. On one hand, this leads to bulging of the central cell cortex, formation of excess area, and fluidization of the cortex in small dKD cells. On the other hand, large dKD cells are prestressed by the contractile small cells and thereby seem to start proliferating. In turn, jamming of the small dKD cells in combination with the uncontrolled proliferation eventually impair collective migration.

4. Discussion

In this study, we were able to show that efficient collective cell migration depends on the tight junction ZO proteins. We show that ZO protein loss leads to severe cellular crowding and eventually jamming, which is fostered by morphological, mechanical, and cytoskeletal integrity loss.

Essentially, we found that ZO protein loss leads to formation of thick and contractile perijunctional actomyosin cables. This is in line with previous characterizations of cells lacking ZO proteins.[1,4,8,11] Particularly, recent evidence suggests that TJs provide a negative mechanical feedback to the actomyosin cytoskeleton of individual cells in a layer, so that they do not contract and pull excessively.[1] Because this feedback loop is missing in our cell lines, it is expected that most individual cells contract in an uncontrolled manner.

Indeed, many cells contract excessively via the perijunctional actomyosin ring. The constriction of this ring leads to laterally smaller cells with a projected area in 2D of about 80 μm^2 that bulge out apically, presumably in order to maintain constant volume. Since actin is remodeled and potentially recruited from the cortex into these rings, the cortex is softened. These observations are in line with recent studies showing similar actomyosin remodeling in conjunction with such morphological changes, particularly of the cell cap.[1,4,8,11] In general, actomyosin remodeling is known to determine cell mechanical as well as morphological adaptations.[42–44] Together, the dome-like apical membrane and the weakened cortex result in excess membrane area accompanied by lower prestress and higher fluidity while the actomyosin ring itself becomes extremely stiff as visible in our force maps.

In contrast to our observations of softening and fluidization of the cell body, former work by Cartagena-Rivera and coworkers report a general tension and viscosity increase in ZO1/2 knockout cells.[2] However, experiments in this study either targeted cell junctions directly or were carried out with much larger probes (> 20 µm) than our conical indenters of only a few

tens of nanometers. Therefore, their measurements are integrated over a larger area capturing the mechanical response from both the extremely stiff cell borders and the soft cell body, which might explain the controversial findings.[2] Another reason could be the fact that the authors used much longer cell growth times than us of over one week. Coupled with the uncontrolled proliferation, this might explain the discrepancies in the observed mechanical behavior: Upon long culturing times, the cell layer becomes increasingly dense, meaning more cells and thereby actin rings per area which, in turn, will dominate the mechanical readout in those studies.

In addition to these contractile small cells, we observe a second phenotype only in cells lacking both ZO1 and 2 (dKD). This second cell phenotype is characterized by: 1) a larger projected area of 150-250 µm^2, i.e., larger than most dKD cells but smaller than average WT cells, 2) thinner perijunctional actomyosin rings, 3) a flattening of the apical cortex, and 4) much higher prestress T_0 and less excess membrane area than the dKD cells. Hence, two mechanically and morphologically distinct but coexisting dKD cell phenotypes emerge with time. For clarity, we distinguish between these two phenotypes and refer to them as *small* and *large* dKD cells.

The perijunctional actin contraction of the small cells is presumably responsible for the flattening and stretching of neighboring cells, which become larger. In response, the large cells need to sacrifice some of the excess area stored in the apical cell membrane, explaining the smaller decrease in K_A in contrast to the smaller dKD cells. Similarly, the pulling force from the contractile small cells is reflected in the increase in T_0 in the large cells.

In essence, the small cells contract and thereby pull on the large cells and stretch them balancing the forces across the cell layer.

However, the large cells are unable to escape from the tensile stress into the third dimension. As a consequence, the cells become laterally stressed and respond by proliferation, which

514 relaxes the lateral stress. In turn, the increased proliferation leads to higher cell densities and
515 eventually to partial jamming, impairing cell migration.
516
517 These observations of uncontrolled proliferation and mechanical imbalances are in line with
518 the idea that TJs are both biological signaling hubs[45,46] and mechanical sensors.[1,3] On one
519 hand, ZO proteins have been shown to directly control proliferation through cell cycle
520 arrest.[47,48] On the other hand, Rosenblatt and coworkers recently showed that mechanically
521 stretched MDCK II cells divide more frequently than unstressed cells.[49] Mechanical stretch
522 itself rapidly stimulates cell proliferation through activation of the Piezo 1 ion channel.[49] We
523 propose that the contractile smaller cells provide exactly this kind of mechanical stimulus
524 leading to cell divisions primarily of the larger, flat cells, which are stretched considerably. A
525 statistical analysis by visual inspection (Figure S5) confirms this hypothesis and shows that
526 larger cells proliferate more frequently, while smaller ones divide less.
527
528 This proliferation and cell density increase coupled with the single cell mechanical changes
529 leads to migration disruption and jamming. Strikingly, evidence accumulates that particularly
530 smaller cells are responsible for the onset of jamming in dKD cells.
531 Specifically, the differences in the jamming expansion of KO and dKD cells, respectively, can
532 only be explained by the area-dependence of active migration on the individual cell area.
533 While the KO and WT cells display the same fast and active dynamics regardless of their cell
534 area, dKD cells become increasingly less dynamic with decreasing cell areas. Particularly, the
535 small dKD cells, which constitute the majority, show passive diffusion-like behavior with a
536 power-law exponent of about 1, whereas the larger cells display active motion with a similar
537 exponent to the WT cells of about 1.8. Accordingly, the small cells are particularly immobile
538 and thereby impairing the migration of the whole dKD layer.

539 Together, these results draw the following picture (**Figure 7**): Small, immobile cells with
540 thick actomyosin rings contract excessively and by that pull on their neighbors, which are
541 laterally strained and flattened displaying a large projected area. The large cells respond to the
542 lateral stress by proliferation leading to even more small cells and crowding.
543

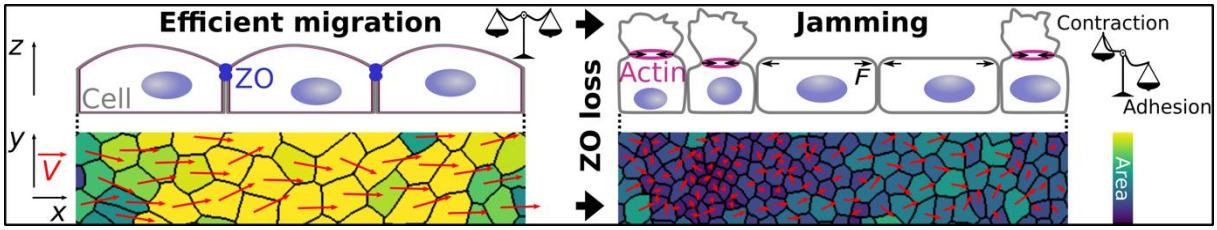

544 **Figure 7**. Proposed model of the delicate force balance necessary for cell layer fluidity. WT
545 cells display a balance equilibrium between contraction and adhesion, and, thus, display a
546 homogenous morphology and can migrate efficiently (left). In contrast, cells lacking ZO
547 proteins develop a new and perturbed force balance leading to heterogeneous cell morphology
548 and jamming (right). Two cell populations emerge: small, highly contractile cells with
549 apically bulged-out excess membrane and large, stretched cells. The small cell population is
550 particularly immobile and additional crowding amplifies this jamming.
551

552 On a mesoscopic scale, both migration velocity and order are diminished in ZO1/2 dKD cells
553 and, upon progressing migration and proliferation, also in ZO1 KO cells. This is in line with
554 recent work showing the deceleration of migration in cells lacking ZO proteins.[5,50] For
555 instance, endothelial cells lacking ZO1 were shown to migrate slower.[5] For MDCK II cells,
556 Fedele et al. found that the migration dynamics of monolayers with already inhibited adherens
557 junctions are diminished upon ZO1/2 double knockout.[50] In addition, ZO protein loss
558 significantly shortens the spatial velocity correlation length. Along the same line, the KO and
559 particularly the dKD monolayers develop more individual leader cells. Both velocity
560 correlation and leader cell emergence were implicated as hallmarks of collective cell behavior

and mechanical coupling.[15,26,31,51,52] Accordingly, cells lacking ZO proteins behave less collectively and exhibit perturbed mechanical coupling.

Yet, since cell mechanics and proliferation are tightly coupled, the relative impact of each on the stalled migration remains to be elucidated. Therefore, we investigated the peculiar relationship between cell mechanics and cell density by inhibiting proliferation. In line with recent studies, proliferation inhibition slightly increases migration speed in WT MDCK cells.[19,21] Strikingly, inhibiting the proliferation of dKD cells succeeds in almost complete recovery of the migration velocity, order, and correlation length observed for WT cells. This underlines the importance of the mechanically induced proliferation and cell crowding as a decisive control parameter for collective migration.

The observation that MDCK cells at low densities show such a high, and at higher densities a significantly lower power-law exponent is shared by recent experimental evidence.[53,54] This general effect of cell density on collective migration dynamics is also in line with physical particle-based models of tissue dynamics.[36] These models predict cell density to be the main determinant parameter for collective motility with motion arrest at high densities. However, to our knowledge, the direct dependence of cell motility of individual cells in a monolayer on their projected area has not been observed experimentally before.

Interestingly, the cell shape (projected aspect ratio in 2D), as predicted by vertex-based models, does not seem to be the decisive parameter in contrast to the cell area itself. Particularly, while we do see a slight shift towards lower overall aspect ratios, we do not observe a clear dependency of the motility of individual cells on the aspect ratio as on the area. It is important to note that instead of addressing the aspect ratio of individual cells, current models focus on the properties of monolayers as a bulk. However, as Devany et al. showed in simulations and experiments that absolute changes of the cell shape can vary greatly and could thus be inconclusive, depending on the experimental situation.[53]

Importantly, Saraswathibhatla and Notbohm found a correlation between cell density, shape, and motility.[54] While we only observe small changes in cell shape, we do observe a similar impact of cell density.

In addition, most studies identifying the cell shape as the predictive parameter for cell motility worked with other cell types and on longer times scales. Typically, fully polarized cells, such as airways smooth muscle cells cultivated for several days and up to weeks, were used, whereas our MDCK II cells only had about 28 h to grow to full (over-)confluence.[20,25,55] Studies working with (ZO protein-inhibited) MDCK or MCF10A lines also cultivated the cells much longer,[2,56] which in conjunction with the observed uncontrolled proliferation could explain the density-related discrepancies. Furthermore, related studies investigated the motion of confluent cell layers, whereas we focused on freely migrating epithelia.[20,25,30,54–56]

An interesting question to be solved will be the emergence mechanism of the two dKD cell phenotypes, comprising extremely small and contractile as well as large and stretched cells. To answer this, targeting single cells or cell clusters within a layer with cytoskeletal drugs, possibly in combination with proliferation inhibition, could be a promising approach in the future.

4. Conclusion

We showed that ZO proteins are not only crucial for barrier function but also for efficient collective cell migration of epithelial monolayers. Our results draw the following picture of the impact of ZO1 and 2 protein loss: Due to missing mechanical feedback from ZO1/2, a thick actomyosin ring builds at the cell periphery that leads to strong contraction of individual cells, constricting the apical cell cortex and leading to in- or outward bulging. Two cell phenotypes emerge in ZO1 and 2 depleted cells after a few hours of migration: 1) Small contractile cells with an apically bulged-out and softened cortex and 2) large, flat cells with an

elevated prestress. The larger cells receive a mechanical stimulus from the highly contractile neighbors and respond by increased proliferation, leading to crowding and, in turn, to even more small cells. Particularly these small cells are rendered immobile and, together with additional crowding, lead to partial jamming of the entire layer.

We conclude that functioning tight junctions are necessary to maintain fluidity of epithelial monolayers and thereby guarantee for fast and coherent cell migration.

5. Material and Methods

Cell culture: Madin-Darby Canine Kidney cells (strain II, MDCK II; European Collection of Authenticated Cell Cultures, Salisbury, UK) were cultured in minimum essential medium (MEM; Life Technologies, Paisley, UK) containing Earle's salts, 2 mM GlutaMAX™ (ThermoFisher Scientific, Waltham, Massachusetts, USA), 2.2 g/L $NaHCO_3$, and 10% fetal bovine serum (FCS; BioWest, Nuaillé, France), called $M10F^-$ in the following, at 37°C and 5% CO_2 in a humidified incubator. The cells were passaged before reaching confluence two to three times per week using phosphate buffered saline pH 7.4 (PBS^-; Biochrom, Berlin, Germany) containing trypsin/EDTA (0.25%/0.02% w/v; BioWest/Biochrom).

Genetic modification of ZO proteins: ZO knockdowns were effected as described in Beutel et al.[40] To knockdown ZO1 and ZO2 in MDCK II cells, frame-shift mutations were introduced at the N-termini by CRISPR/Cas9. The following RNA guides (gRNA) were used for ZO1: ACACACAGTGACGCTTCACA and ZO2: GTACACTGTGACCCTACAAA. Selected DNA oligos and their trans-encoded RNA (TRCR) were purchased from Integrated DNA Technologies. Each gRNA was annealed for 1h at room temperature with its TRCR. To finally generate the riboprotein complex, the gRNA/TRCR complex was incubated with homemade purified Cas9. Electroporation of each complex was performed in 300,000 cells (Invitrogen NEON electroporation machine and kit, 2 pulses, 20 ns, 1200 V). Single cells

were sorted after 48 h by FACS (fluorescence activated cell sorting) and grown clonally. The genomic sequence of the genes of interests were sequenced and only clones carrying homozygous frame-shifts leading to an early stop codon were kept. To generate a combined ZO1/ZO2 knockdown KD line, we first created a ZO1 knockout and then we targeted ZO2. The ZO1 KO clone was mutant for two alleles, both alleles have a 1 bp insertion in the guide region (ACACACAGTGACGCTTC-1 bp insertion-ACAGGG) leading to an early stop of translation. The ZO2 KD has 5 bp deletion at the end of the guide region (GTACACTGTGACCCTACA-5 bp deletion-GG) leading to an early stop. Immunostaining and western-blot analysis showed that ZO1 and ZO2 presented a residual expression level of the full-length protein equal to 2-3% of the WT line expression level (Beutel et al FigS5).

Cell migration experiments: For migration experiments Petri dishes with a culture-insert (Culture-Insert 2 Well in µ-Dish 35 mm, ibiTreat #1.5 polymer cover slip; ibidi, Martinsried, Germany) were used. Cells were seeded at $4 \cdot 10^5$ cells in 1 mL M10F$^-$ on the outside of the insert and grown to (over-) confluence for 28 h (± 1.5 h). Upon visual inspection, the insert was removed, the cells were rinsed with M10F$^-$, supplied with sufficient M10F$^-$ (2-3 mL), and placed into the incubation system of an inverted optical microscope (BZ-X810; Keyence, Neu-Isenburg, Germany) equipped with a 10X phase contrast objective (Nikon CFI60 Series; Keyence). The temperature was calibrated to be 37°C at the cell sample using a local temperature measurement instrument (Testo 735; Testo, Lenzkirch, Germany), a partial CO_2 pressure of 5% was chosen, and sufficient humidity was ensured by injecting distilled water into the incubator appliance. Phase contrast frames were recorded at 1 frame/2.5 min, 14 bit, 25% illumination power, typical exposure times of about 1/25 s, and without zoom, gain, or binning. Focus tracking was applied and three vertical slices were chosen in a range of 5 µm to avoid drift effects. The cell edge was carefully aligned vertically and set to be at a similar position for all experiments. Typically, migration was observed overnight for 20-30 h.

Mitomycin C treatment: Mitomycin C (MitoC; Sigma-Aldrich, Steinheim, Germany) was dissolved in DMSO to reach 500 µg mL^{-1} and stored in aliquots of 150 µL.

Cell seeding was performed as described above. The samples were rinsed once and then incubated with $M10F^-$ containing 10 µg mL^{-1} of Mitomycin C at 37°C and 5% CO2 for 1 h. Then, the insert was removed after about 28 h growth time (± 1.5 h). To remove any extruded cells and, most importantly, to prevent the cytotoxic effects of Mytomycin C occurring after 12 h of exposure,[18] samples were rinsed with 1 mL $M10F^-$ three times, before the dishes were filled with 2-3 mL $M10F^-$ and then imaged as described above.

Experiments with non-migrating monolayers: 5 10^5 cells were seeded in 4mL $M10F^-$ and placed immediately on the same microscope as above and the same conditions as for the migration experiments were used but without an insert. Four areas per sample were imaged every hour with the same settings as above. Two WT samples, one KO and one dKD sample were recorded. Analysis was performed as described below.

Migration data analysis: First, migration phase contrast movies were down-sampled to 1 frame/7.5 min to ensure good PIV (particle image velocimetry) quality. Velocity vector maps were obtained using the Matlab (MathWorks, Natick, USA) -based PIV tool AVeMap from Deforet et al.[34] A window size of 32 x 32 pixels corresponding to 24.16 µm x 24.16 µm with an overlap of 0.5 was used, yielding a vector mesh size of 16 pixels (12.08 µm). The first row width was set to 12.08 µm and typical mask parameters were 0.60-0.75. The default filters of 1.1 signal-to-noise ratio, 0.3 peak height, and 4 global filtering were used. A PIV quality of > 0.8 was achieved for all data and exemplarily checked by visual inspection. The order parameter was defined as $\cos\alpha$, where α is the angle between the local velocity vector and the normal to the average migration direction. The add-on AVeMap+ was used to analyze

691 the data with respect to the distance from the migration edge. Note, the first two to three data
692 points are not shown due to a known edge-induced artefact.[57]
693 Vector fields were further analyzed using home-written Python scripts. Before correlation
694 functions were calculated, the leader cell fingers were cut from the vector fields to yield
695 rectangular input data for the spatial correlation and to avoid edge-induced artifacts.
696 The correlation function was calculated for each time point individually as the 2D spatial
697 autocorrelation *AC* of the velocity vector field using the Scipy function signal.correlate2d and
698 according to Petitjean et al.:[31,58]

699 $$AC(\vec{r},t) = \langle v(\vec{r}' + \vec{r},t) \times v(\vec{r}',t)\rangle$$

700 With the deviation of the *y*-component (perpendicular to the migration direction) $v = v_i -$
701 $\langle v\rangle$, which is corrected by the offset $\langle v\rangle$, of the vector $\vec{r}$ at time point t. The brackets denote
702 averaging over all vectors. Additionally, the *AC* is normalized by its maximum, so that it
703 starts from one.
704 To gain a one-dimensional function, the 2D correlation function was then radially averaged in
705 space. The correlation function was finally averaged for each migration movie over time.
706 The correlation length was defined as the integral over the weighted spatial correlation
707 function $AC(r)$:

708 $$\int_0^\infty \vec{r} \cdot AC(\vec{r})\, d\vec{r}$$

709 To exclude any anti-correlation artifacts ($AC < 0$) at large distances, we only integrated up to
710 the x-intercept for all analyses.
711 The amount of leader cells was determined from the phase contrast movies manually. Leader
712 cells were defined by their position at a protrusion in the front of the leading edge, an
713 increased cell size compared with bulk cells, and a lamellipodium towards the empty space.
714

Automated cell segmentation: The deep learning-based cell segmentation algorithm Cellpose (Stringer et al.[35]) was used to extract a mask and an outline for each individual cell body in an image. The model type was set to *cyto* and the grayscale phase contrast images were used as input. Before segmentation, the image contrast was auto-corrected using Fiji to facilitate optimal cell recognition.[59] In order to accurately capture all cells in the layer, the flow and cell probability thresholds were set to 1 and -6, respectively. We found these parameters to be optimal for our images, because smaller (or larger, respectively) values resulted in missed cells. No novel model training was necessary. The input diameter was estimated automatically for every image individually by the software.

Cell area, position, and aspect ratio calculation and processing: For every segmented image, the masks array and the outlines array were extracted from the returned segmentation dictionary. The arrays were normalized, so that ones specified cell bodies (or cell outlines) and zeros empty space, respectively. The outlines were subtracted from the masks to prevent overlap of cells. The resulting array was converted into the data type uint8 and scaled up to a value of 255. The array was then subjected to a threshold at a value of 127 and binarized using the image processing library OpenCV.[60] The arrays were then transposed into vectors of coordinates specifying the outer contour of each cell using the function *findContours* of OpenCV.[60] Only outer contours were extracted and the Teh-Chin chain approximation algorithm was applied to save memory.[61] On the basis of the extracted vectors, the area of each cell was computed using the function contourArea of OpenCV. The moments function was used to determine the center of each cell, yielding the positions later used by Trackpy. Cell density was calculated dividing the number of segmented cells by the area occupied by the monolayer (either the mask obtained from AVeMap or the whole field of view).

To determine cell aspect ratios (length/width), two approaches were utilized to define the front-rear (anterior-posterior) axis for each individual cell. First, the fitEllipse function of OpenCV was used for every given set of coordinates to compute and fit an ellipse to the 2D points. Since this function works by fitting the coordinates in a least-squares approach, it was found that the algorithm seemed to be biased towards high aspect ratios for some cell shapes. Therefore, the function minAreaRect was used to verify the results by calculating a rotated minimum-area rectangle enclosing the respective set of coordinates. This procedure, however, seemed to be biased towards low aspect ratios for the aforementioned cell shapes. Accordingly, we computed the aspect ratio with both algorithms independently and then used the mean for every cell in each image individually. The validity of this approach was verified by visual inspection of overlaid input and output images.

Single cell tracking and analysis: Single cell tracking was performed with the cell positions calculated before by the OpenCV moments function (*vide supra*). Trackpy was used to link the cell positions, yielding individual tracks.[62,63] Input data were the segmented phase contrast time series between 19 and 21 h at a temporal resolution of 1 frame/7.5 min. The link function was used with a memory of 4 frames and 10 pixels as maximal displacement. The resulting trajectories were filtered, so that only the ones that persisted for at least 5 frames were kept, to avoid spurious trajectories. No drift correction was necessary.
Mean-square-displacements (*MSD*s) were calculated using the ensemble *MSD* function of Trackpy as:

$$MSD(\tau) = \langle (x(t+\tau) - x(t))^2 \rangle$$

The brackets denote averaging over time and over all cells. Before calculation and fitting of the *MSD*s, the trajectories were filtered by discrete bins of 100 µm^2 cell area (see Figure 2 and 3) or 0.25 aspect ratio (see Figure S1 and S2). *MSD*s were fitted by a power law of the form

765 $MSD(\tau) = a\,\tau^n$ with a power law exponent *n* and an offset *a* using a linear regression in
766 logarithmic space implemented in Trackpy.
767
768 *AFM-based force spectroscopy*: Force spectroscopic indentation measurements were carried
769 out with a NanoWizard 4 (JPK Instruments, Berlin, Germany) mounted on an inverted
770 microscope (IX 81; Olympus, Tokyo, Japan) using silicon nitride cantilevers with a nominal
771 spring constant of 0.01 N m^{-1} (MLCT C; Bruker AFM Probes, Camarillo, USA). Before an
772 experiment, cantilevers were rinsed with isopropanol and PBS^- as well as incubated with
773 FITC-conjugated Concanavalin A solution (2.5 mg mL^{-1} in PBS^-; Sigma-Aldrich) for 1 h.
774 The sensitivity of the AFM was determined by recording force curves in the empty space
775 without cells and the exact spring constant of each cantilever was determined by the thermal
776 noise method.[64] Approximately 20 h after removing the insert (*vide supra*), cells were rinsed
777 three times with $M10F^-$ containing 0.2 mg mL^{-1} Penicillin (Biochrom), 0.2 mg mL^{-1}
778 Streptomycin (Biochrom), and 15 mM HEPES ($M10F^+$; BioWest).
779 For the measurements, samples were mounted on the AFM stage, 2.5 mL $M10F^+$ was
780 supplied, and the heater (JPK Instruments) was set to 37°C. The cells were indented at a
781 constant speed of 2 µm s^{-1} to maximum force of 1 nN. After a dwell time of 0.5 s at constant
782 height the indenter was retracted at the same speed. Force maps of 25 pixels x 25 pixels in an
783 area of 50 µm x 50 µm were recorded by lateral scanning across the sample recording one
784 force indentation cycle at each pixel. Additionally, five consecutive force curves in the center
785 of individual cells in the monolayer were acquired using the same parameters.
786
787 *Force curve analysis and mechanical model*: Generally, force-relaxation curves were
788 recorded as detailed previously.[41] After indentation of the center of the cell with a velocity of
789 2 µm s^{-1} to avoid artefacts from hydrodynamic drag acting on the cantilever, we switched off
790 the constant force feedback loop and kept the system at constant height. During this time the

decrease of cantilever deflection is monitored as a function of time (for 0.5 s). We used the same MLCT-C cantilevers as for imaging (*vide infra*). The curves were modeled using a theory introduced recently.[41,65] Briefly, the surfaces of the confluent MDCK II cells are described as capped cylinders. The average geometry as derived from AFM imaging was employed to describe the apical cap of the deformed cells in terms of contact angle and radius of the basis. Generally, we consider the cell as a liquid-filled object surrounded by an isotropic viscoelastic shell deformed at constant volume. The force F acting on the apex of the cell is given by:

$$F = 2\pi \left({R_1}^2 \left(\frac{R_1 \sin\phi + r_1 \sin\theta}{{R_1}^2 {r_1}^2} \right) - R_1 \sin\phi \right) T(t)$$

with R_1, the radius at the base of the spherical cap and ϕ the contact angle in response to deformation. r_1 is the contact radius with the conical indenter, $\theta = \frac{\pi}{2} - \vartheta$ with ϑ, the cone half angle.

Viscoelasticity of the shell enters the tension term $T(t)$ through a time dependent area compressibility modulus $K_A = {K_A}^0 (t/t_0)^{-\beta}$. Now we need to solve a set of nonlinear equations for the shape of the deformed cell to fulfill force balances and the constant volume boundary condition. The resulting shapes are minimal surfaces to minimize the stretching energy. Membrane tension T_t was calculated from the tether rupture force F_t at the end of the retraction curve via $T_t = \frac{F_t^2}{8\pi^2 \kappa}$ with the bending modulus $\kappa = 2.7 \cdot 10^{-19}$ J.[66–68]

Analysis was performed using self-written Python and Matlab scripts in combination with the JPK SPM Data Processing (JPK Instruments / Bruker) software. The baseline was corrected by a linear fit before contact. The contact point was determined individually using the JPK SPM Data Processing. Tether forces were acquired with the same software.

AFM imaging: Approximately 20 h after removing the insert (*vide supra*), cells were rinsed three times with PBS containing 0.1 g L^{-1} Mg^{2+} and 0.133 g L^{-1} Ca^{2+} (PBS^{++}; Sigma-Aldrich) and incubated with glutaraldehyde solution (2.5% (v/v) in PBS^{++}) for 20 min. PBS^{++} was used instead of PBS without magnesium and calcium ions, because the dKD and KO cells were more prone to dissolution of ion-dependent adhesions due to the missing diffusion barrier function. Before imaging, the samples were rinsed again three times to remove residual GDA. Cell imaging was performed using a NanoWizard III (JPK Instruments) mounted on an inverted optical microscope (IX 81; Olympus) to enable additional visual inspection via phase contrast. Imaging was carried out as described in Brückner et al.[43] in contact mode using MLCT C cantilevers (Bruker AFM Probes) in PBS^{++} with typical line scan rates of about 0.3 Hz and typical forces of 0.1 nN. Height and error images were obtained using the JPK SPM Data Processing software provided by the manufacturer.

Cell labeling and fluorescence microscopy: Prior to cell labeling, cells were fixed by incubation with paraformaldehyde/glutaraldehyde solution (4% (w/v)/0.1% (w/v) in PBS^{++}; Science Services, Munich, Germany/Sigma-Aldrich) for 20 min. To permeabilize the cellular plasma membrane, samples were incubated with 0.1% (v/v) Triton X-100 in PBS^{-} for 5 min. After three rinsing steps with 1 mL PBS^{++} each, to block unspecific binding sites, cells were incubated with blocking/dilution buffer (PBS^{-} containing 2% (w/v) bovine serum albumin and 0.1% (v/v) Tween20) for 30 min.

For ZO1 staining, a fluorophore-conjugated primary antibody (mouse ZO1-1A12 IgG1 AlexaFluor 488; Invitrogen, ThermoFisher Scientific, Waltham, Massachusetts, USA) was diluted with blocking/dilution buffer to a concentration of 5 µg mL^{-1} and cells were incubated for 1 h. For all other proteins, the following primary antibodies were diluted in blocking/dilution buffer.

841 *ZO2*: 1 µg mL^{-1} Clone 3E8D9 mouse IgG1; Invitrogen. Phospho-Myosin: 1:200 light chain 2
842 (Ser 19) rabbit IgG1; Cell Signaling Technology, Danvers, Massachusetts, USA. *E-Cadherin*:
843 1:50 Clone 36 mouse IgG1; BD Biosciences, Heidelberg, Germany. *ß-catenin*: 5 µg mL^{-1}
844 mouse IgG1; BD Biosciences. *Occludin*: 6.5 µg mL^{-1} EPR20992 rabbit IgG; Abcam,
845 Cambridge, UK. Claudin 1: 11.6 µg mL^{-1} rabbit IgG; Abcam.
846 After the primary antibody, cells were rinsed briefly with PBS^{++}, and then washed with
847 PBS^{++}, with 0.1% (v/v) Triton X-100 in PBS^{-} and again with PBS^{++} for 5 min each on a
848 shaker plate (75 rpm). The secondary antibody (AlexaFluor 488- or AlexaFluor 546-
849 conjugated goat anti-mouse or anti-rabbit IgG; Life Technologies, Carlsbad, USA) was
850 diluted with blocking/dilution buffer to a concentration of 5 µg mL^{-1}. The cells were
851 incubated for 1 h. Actin labeling was performed using AlexaFluor 488- or AlexaFluor 546-
852 phalloidin (Invitrogen), diluted together with the secondary antibody in blocking/dilution
853 buffer to a concentration of 165 nM. Incubation time: 45 min. Following the secondary
854 antibody, samples were washed with PBS^{++} for 5 min each on a shaker plate (75 rpm).
855 Nucleus staining was performed by incubation with Hoechst 33342 (Invitrogen), diluted to
856 1 µg mL^{-1}, for 15 min. For imaging, samples were rinsed three times with PBS^{++} and kept in
857 PBS^{++}. All labeling steps were performed at room temperature.
858 A confocal laser scanning microscope (FluoView1200; Olympus, Tokyo, Japan), equipped
859 with a 60X oil immersion objective (*NA* = 1.25), was used for fluorescence imaging. Image
860 processing, brightness adjustment, and analysis was performed using Fiji.[59]
861
862 *Statistical analyses*: The data were tested for normality using the Shapiro-Wilk test. Because
863 for none of the migration-related data the null hypothesis of a normal distribution was rejected
864 (at the $p < 0.05$ level), significance was tested using Welch's t-test. The Mann-Whitney U test
865 was applied to the AFM data to accommodate non-normality. All statistical analyses were
866 performed in Python.

A p-value of < 0.05 was considered significant and denoted by one asterisk (*), $p < 0.01$ and $p < 0.001$ we indicated by two (**) and three (***) asterisks, respectively.

Supporting Information

Supporting Information is available at the end of this document.

Acknowledgements

Funding by the DFG though grants SPP1782 and DFG JA963 is gratefully acknowledged. We thank Jonathan F.E. Bodenschatz for technical assistance and discussions. We would also like to acknowledge Filip Savić, for his help with the PIV analyses and Burkhard Geil for the helpful discussions about the segmentation and tracking.

M.S., H.P., M.F., J.G., and A.R. executed measurements and performed analyses. M.S. designed and planned the experiments. R.M. and A.H. carried out the genetic modifications. T.O., A.H., and A.J. designed and supervised the research. M.S. and A.J. wrote the manuscript. All authors helped with discussions and proofreading.

References

[1] G. Hatte, C. Prigent, J.-P. Tassan, *J Cell Sci* **2018**, *131*, DOI 10.1242/jcs.208736.
[2] A. X. Cartagena-Rivera, C. M. V. Itallie, J. M. Anderson, R. S. Chadwick, *Nat Commun* **2017**, *8*, 1.
[3] D. Spadaro, S. Le, T. Laroche, I. Mean, L. Jond, J. Yan, S. Citi, *Current Biology* **2017**, *27*, 3783.
[4] W. Choi, B. R. Acharya, G. Peyret, M.-A. Fardin, R.-M. Mège, B. Ladoux, A. S. Yap, A. S. Fanning, M. Peifer, *J Cell Biol* **2016**, *213*, 243.
[5] O. Tornavaca, M. Chia, N. Dufton, L. O. Almagro, D. E. Conway, A. M. Randi, M. A. Schwartz, K. Matter, M. S. Balda, *J Cell Biol* **2015**, *208*, 821.
[6] S. Citi, *Biophysical Reviews* **2019**, DOI 10.1007/s12551-019-00582-7.
[7] M. A. Odenwald, W. Choi, W.-T. Kuo, G. Singh, A. Sailer, Y. Wang, L. Shen, A. S. Fanning, J. R. Turner, *Journal of Biological Chemistry* **2018**, *293*, 17317.
[8] M. A. Odenwald, W. Choi, A. Buckley, N. Shashikanth, N. E. Joseph, Y. Wang, M. H. Warren, M. M. Buschmann, R. Pavlyuk, J. Hildebrand, B. Margolis, A. S. Fanning, J. R. Turner, *J Cell Sci* **2017**, *130*, 243.
[9] A. S. Fanning, B. J. Jameson, L. A. Jesaitis, J. M. Anderson, *J Biol Chem* **1998**, *273*, 29745.
[10] A. S. Fanning, C. M. Van Itallie, J. M. Anderson, *MBoC* **2011**, *23*, 577.
[11] S. Tokuda, T. Higashi, M. Furuse, *PLoS ONE* **2014**, *9*, e104994.

[12] S. Jain, V. M. L. Cachoux, G. H. N. S. Narayana, S. de Beco, J. D'Alessandro, V. Cellerin, T. Chen, M. L. Heuzé, P. Marcq, R.-M. Mège, A. J. Kabla, C. T. Lim, B. Ladoux, *Nature Physics* **2020**, DOI 10.1038/s41567-020-0875-z.
[13] R. Sunyer, V. Conte, J. Escribano, A. Elosegui-Artola, A. Labernadie, L. Valon, D. Navajas, J. M. Garcia-Aznar, J. J. Munoz, P. Roca-Cusachs, X. Trepat, *Science* **2016**, *353*, 1157.
[14] M. Reffay, M. C. Parrini, O. Cochet-Escartin, B. Ladoux, A. Buguin, S. Coscoy, F. Amblard, J. Camonis, P. Silberzan, *Nature Cell Biology* **2014**, *16*, 217.
[15] E. Anon, X. Serra-Picamal, P. Hersen, N. C. Gauthier, M. P. Sheetz, X. Trepat, B. Ladoux, *Proceedings of the National Academy of Sciences* **2012**, *109*, 10891.
[16] X. Trepat, M. R. Wasserman, T. E. Angelini, E. Millet, D. A. Weitz, J. P. Butler, J. J. Fredberg, *Nature Physics* **2009**, *5*, 426.
[17] M. Poujade, E. Grasland-Mongrain, A. Hertzog, J. Jouanneau, P. Chavrier, B. Ladoux, A. Buguin, P. Silberzan, *Proceedings of the National Academy of Sciences* **2007**, *104*, 15988.
[18] E. Gauquelin, S. Tlili, C. Gay, G. Peyret, R.-M. Mège, M. A. Fardin, B. Ladoux, *Soft Matter* **2019**, *15*, 2798.
[19] L. Atia, D. Bi, Y. Sharma, J. A. Mitchel, B. Gweon, S. A. Koehler, S. J. DeCamp, B. Lan, J. H. Kim, R. Hirsch, A. F. Pegoraro, K. H. Lee, J. R. Starr, D. A. Weitz, A. C. Martin, J.-A. Park, J. P. Butler, J. J. Fredberg, *Nature Physics* **2018**, *14*, 613.
[20] S. Tlili, E. Gauquelin, B. Li, O. Cardoso, B. Ladoux, H. Delanoë-Ayari, F. Graner, *Royal Society Open Science* **2018**, *5*, 172421.
[21] C. Malinverno, S. Corallino, F. Giavazzi, M. Bergert, Q. Li, M. Leoni, A. Disanza, E. Frittoli, A. Oldani, E. Martini, T. Lendenmann, G. Deflorian, G. V. Beznoussenko, D. Poulikakos, K. H. Ong, M. Uroz, X. Trepat, D. Parazzoli, P. Maiuri, W. Yu, A. Ferrari, R. Cerbino, G. Scita, *Nature Materials* **2017**, *16*, 587.
[22] D. Bi, X. Yang, M. C. Marchetti, M. L. Manning, *Physical Review X* **2016**, *6*, DOI 10.1103/PhysRevX.6.021011.
[23] J. Notbohm, S. Banerjee, K. J. C. Utuje, B. Gweon, H. Jang, Y. Park, J. Shin, J. P. Butler, J. J. Fredberg, M. C. Marchetti, *Biophys. J.* **2016**, *110*, 2729.
[24] J.-A. Park, J. H. Kim, D. Bi, J. A. Mitchel, N. T. Qazvini, K. Tantisira, C. Y. Park, M. McGill, S.-H. Kim, B. Gweon, J. Notbohm, R. Steward Jr, S. Burger, S. H. Randell, A. T. Kho, D. T. Tambe, C. Hardin, S. A. Shore, E. Israel, D. A. Weitz, D. J. Tschumperlin, E. P. Henske, S. T. Weiss, M. L. Manning, J. P. Butler, J. M. Drazen, J. J. Fredberg, *Nature Materials* **2015**, *14*, 1040.
[25] S. Garcia, E. Hannezo, J. Elgeti, J.-F. Joanny, P. Silberzan, N. S. Gov, *PNAS* **2015**, *112*, 15314.
[26] E. Bazellières, V. Conte, A. Elosegui-Artola, X. Serra-Picamal, M. Bintanel-Morcillo, P. Roca-Cusachs, J. J. Muñoz, M. Sales-Pardo, R. Guimerà, X. Trepat, *Nature Cell Biology* **2015**, *17*, 409.
[27] M. Sadati, N. Taheri Qazvini, R. Krishnan, C. Y. Park, J. J. Fredberg, *Differentiation* **2013**, *86*, 121.
[28] D. T. Tambe, C. Corey Hardin, T. E. Angelini, K. Rajendran, C. Y. Park, X. Serra-Picamal, E. H. Zhou, M. H. Zaman, J. P. Butler, D. A. Weitz, J. J. Fredberg, X. Trepat, *Nature Materials* **2011**, *10*, 469.
[29] T. E. Angelini, E. Hannezo, X. Trepat, M. Marquez, J. J. Fredberg, D. A. Weitz, *Proceedings of the National Academy of Sciences* **2011**, *108*, 4714.
[30] L. Petitjean, M. Reffay, E. Grasland-Mongrain, M. Poujade, B. Ladoux, A. Buguin, P. Silberzan, *Biophysical Journal* **2010**, *98*, 1790.
[31] D. Du, F. Xu, L. Yu, C. Zhang, X. Lu, H. Yuan, Q. Huang, F. Zhang, H. Bao, L. Jia, X. Wu, X. Zhu, X. Zhang, Z. Zhang, Z. Chen, *Developmental Cell* **2010**, *18*, 52.
[32] A. Raya-Sandino, A. Castillo-Kauil, A. Domínguez-Calderón, L. Alarcón, D. Flores-Benitez, F. Cuellar-Perez, B. López-Bayghen, B. Chávez-Munguía, J. Vázquez-Prado, L. González-Mariscal, *Biochimica et Biophysica Acta (BBA) - Molecular Cell Research* **2017**, *1864*, 1714.
[33] M. Deforet, M. C. Parrini, L. Petitjean, M. Biondini, A. Buguin, J. Camonis, P. Silberzan, *Nature Methods* **2012**, *9*, 1081.
[34] C. Stringer, T. Wang, M. Michaelos, M. Pachitariu, *Nature Methods* **2020**, 1.
[35] S. Henkes, Y. Fily, M. C. Marchetti, *Physical Review E* **2011**, *84*, DOI 10.1103/PhysRevE.84.040301.

[36] M. L. Heuzé, G. H. N. Sankara Narayana, J. D'Alessandro, V. Cellerin, T. Dang, D. S. Williams, J. C. Van Hest, P. Marcq, R.-M. Mège, B. Ladoux, *eLife* **2019**, *8*, e46599.
[37] W. Xi, S. Sonam, T. Beng Saw, B. Ladoux, C. Teck Lim, *Nat Commun* **2017**, *8*, DOI 10.1038/s41467-017-01390-x.
[38] V. N. Iyer, W. Szybalski, *Proc Natl Acad Sci U S A* **1963**, *50*, 355.
[39] O. Beutel, R. Maraspini, K. Pombo-García, C. Martin-Lemaitre, A. Honigmann, *Cell* **2019**, *179*, 923.
[40] A. Cordes, H. Witt, A. Gallemí-Pérez, B. Brückner, F. Grimm, M. Vache, T. Oswald, J. Bodenschatz, D. Flormann, F. Lautenschläger, M. Tarantola, A. Janshoff, *Phys. Rev. Lett.* **2020**, *125*, 068101.
[41] C. Guillot, T. Lecuit, *Science* **2013**, *340*, 1185.
[42] B. R. Brückner, H. Nöding, M. Skamrahl, A. Janshoff, *Progress in Biophysics and Molecular Biology* **2019**, *144*, 77.
[43] M. Skamrahl, H. Colin-York, L. Barbieri, M. Fritzsche, *Small* **2019**, *15*, 1902202.
[44] C. Zihni, M. S. Balda, K. Matter, *J Cell Sci* **2014**, *127*, 3401.
[45] L. González-Mariscal, R. Tapia, D. Chamorro, *Biochimica et Biophysica Acta (BBA) - Biomembranes* **2008**, *1778*, 729.
[46] T. Sourisseau, A. Georgiadis, A. Tsapara, R. R. Ali, R. Pestell, K. Matter, M. S. Balda, *Molecular and Cellular Biology* **2006**, *26*, 2387.
[47] C. T. Capaldo, S. Koch, M. Kwon, O. Laur, C. A. Parkos, A. Nusrat, *MBoC* **2011**, *22*, 1677.
[48] S. Gudipaty, J. Lindblom, P. Loftus, M. Redd, K. Edes, C. Davey, V. Krishnegowda, J. Rosenblatt, *Nature* **2017**, *543*, 118.
[49] C. Fedele, E. Mäntylä, B. Belardi, T. Hamkins-Indik, S. Cavalli, P. A. Netti, D. A. Fletcher, S. Nymark, A. Priimagi, T. O. Ihalainen, *Scientific Reports* **2020**, *10*, 15329.
[50] M. Vishwakarma, J. Di Russo, D. Probst, U. S. Schwarz, T. Das, J. P. Spatz, *Nature Communications* **2018**, *9*, DOI 10.1038/s41467-018-05927-6.
[51] S. Rausch, T. Das, J. R. Soiné, T. W. Hofmann, C. H. Boehm, U. S. Schwarz, H. Boehm, J. P. Spatz, *Biointerphases* **2013**, *8*, 32.
[52] J. Devany, D. M. Sussman, M. L. Manning, M. L. Gardel, *bioRxiv* **2020**, 804294.
[53] A. Saraswathibhatla, J. Notbohm, *Physical Review X* **2020**, *10*, DOI 10.1103/PhysRevX.10.011016.
[54] J. A. Mitchel, A. Das, M. J. O'Sullivan, I. T. Stancil, S. J. DeCamp, S. Koehler, J. P. Butler, J. J. Fredberg, M. A. Nieto, D. Bi, J.-A. Park, *bioRxiv* **2019**, DOI 10.1101/665018.
[55] J. H. Kim, A. F. Pegoraro, A. Das, S. A. Koehler, S. A. Ujwary, B. Lan, J. A. Mitchel, L. Atia, S. He, K. Wang, D. Bi, M. H. Zaman, J.-A. Park, J. P. Butler, K. H. Lee, J. R. Starr, J. J. Fredberg, *Biochemical and Biophysical Research Communications* **2020**, *521*, 706.
[56] X. Serra-Picamal, V. Conte, R. Vincent, E. Anon, D. T. Tambe, E. Bazellieres, J. P. Butler, J. J. Fredberg, X. Trepat, *Nature Physics* **2012**, *8*, 628.
[57] P. Virtanen, R. Gommers, T. E. Oliphant, M. Haberland, T. Reddy, D. Cournapeau, E. Burovski, P. Peterson, W. Weckesser, J. Bright, S. J. van der Walt, M. Brett, J. Wilson, K. J. Millman, N. Mayorov, A. R. J. Nelson, E. Jones, R. Kern, E. Larson, C. J. Carey, İ. Polat, Y. Feng, E. W. Moore, J. VanderPlas, D. Laxalde, J. Perktold, R. Cimrman, I. Henriksen, E. A. Quintero, C. R. Harris, A. M. Archibald, A. H. Ribeiro, F. Pedregosa, P. van Mulbregt, *Nature Methods* **2020**, *17*, 261.
[58] J. Schindelin, I. Arganda-Carreras, E. Frise, V. Kaynig, M. Longair, T. Pietzsch, S. Preibisch, C. Rueden, S. Saalfeld, B. Schmid, J.-Y. Tinevez, D. J. White, V. Hartenstein, K. Eliceiri, P. Tomancak, A. Cardona, *Nature Methods* **2012**, *9*, 676.
[59] G. BRADSKI, *Dr Dobb's J. Software Tools* **2000**, *25*, 120.
[60] C.- Teh, R. T. Chin, *IEEE Transactions on Pattern Analysis and Machine Intelligence* **1989**, *11*, 859.
[61] Dan Allan, Casper van der Wel, Nathan Keim, Thomas A Caswell, Devin Wieker, Ruben Verweij, Chaz Reid, Thierry, Lars Grueter, Kieran Ramos, apiszcz, zoeith, Rebecca W Perry, François Boulogne, Prashant Sinha, pfigliozzi, Nicolas Bruot, Leonardo Uieda, Jan Katins, Hadrien Mary, Aron Ahmadia, *Soft-Matter/Trackpy: Trackpy v0.4.2*, Zenodo, **2019**.
[62] J. C. Crocker, D. G. Grier, *Journal of Colloid and Interface Science* **1996**, *179*, 298.

[63] J. L. Hutter, J. Bechhoefer, *Review of Scientific Instruments* **1993**, *64*, 1868.
[64] H. Hubrich, I. P. Mey, B. R. Brückner, P. Mühlenbrock, S. Nehls, L. Grabenhorst, T. Oswald, C. Steinem, A. Janshoff, *Nano Letters* **2020**, DOI 10.1021/acs.nanolett.0c01769.
[65] J. Dai, M. P. Sheetz, *Biophysical Journal* **1999**, *77*, 3363.
[66] F. Brochard-Wyart, N. Borghi, D. Cuvelier, P. Nassoy, *PNAS* **2006**, *103*, 7660.
[67] A. Pietuch, B. R. Brückner, T. Fine, I. Mey, A. Janshoff, *Soft Matter* **2013**, *9*, 11490.

In this article it is shown that tight junction ZO proteins maintain epithelial cell sheet fluidity and thereby ensure efficient and coherent migration. Cells lacking these proteins loose viscoelastic tissue integrity due to actomyosin remodeling and increase proliferation, which induces cellular crowding. Particularly, upon ZO protein loss small cells at high cell densities eventually impair migration and cause jamming.

Mark Skamrahl, Hongtao Pang, Maximilian Ferle, Jannis Gottwald, Angela Rübeling, Riccardo Maraspini, Alf Honigmann, Tabea A. Oswald, and Andreas Janshoff**

Tight junction ZO proteins maintain tissue fluidity, ensuring efficient collective cell migration

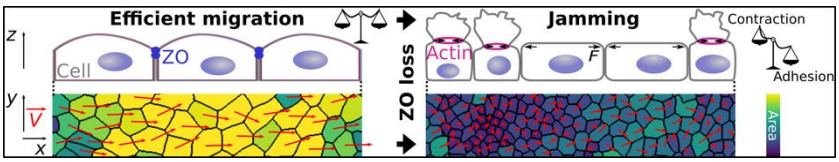

ToC figure

Supporting Information

Tight junction ZO proteins maintain tissue fluidity, ensuring efficient collective cell migration

Mark Skamrahl, Hongtao Pang, Maximilian Ferle, Jannis Gottwald, Angela Rübeling, Riccardo Maraspini, Alf Honigmann, Tabea A. Oswald, and Andreas Janshoff**

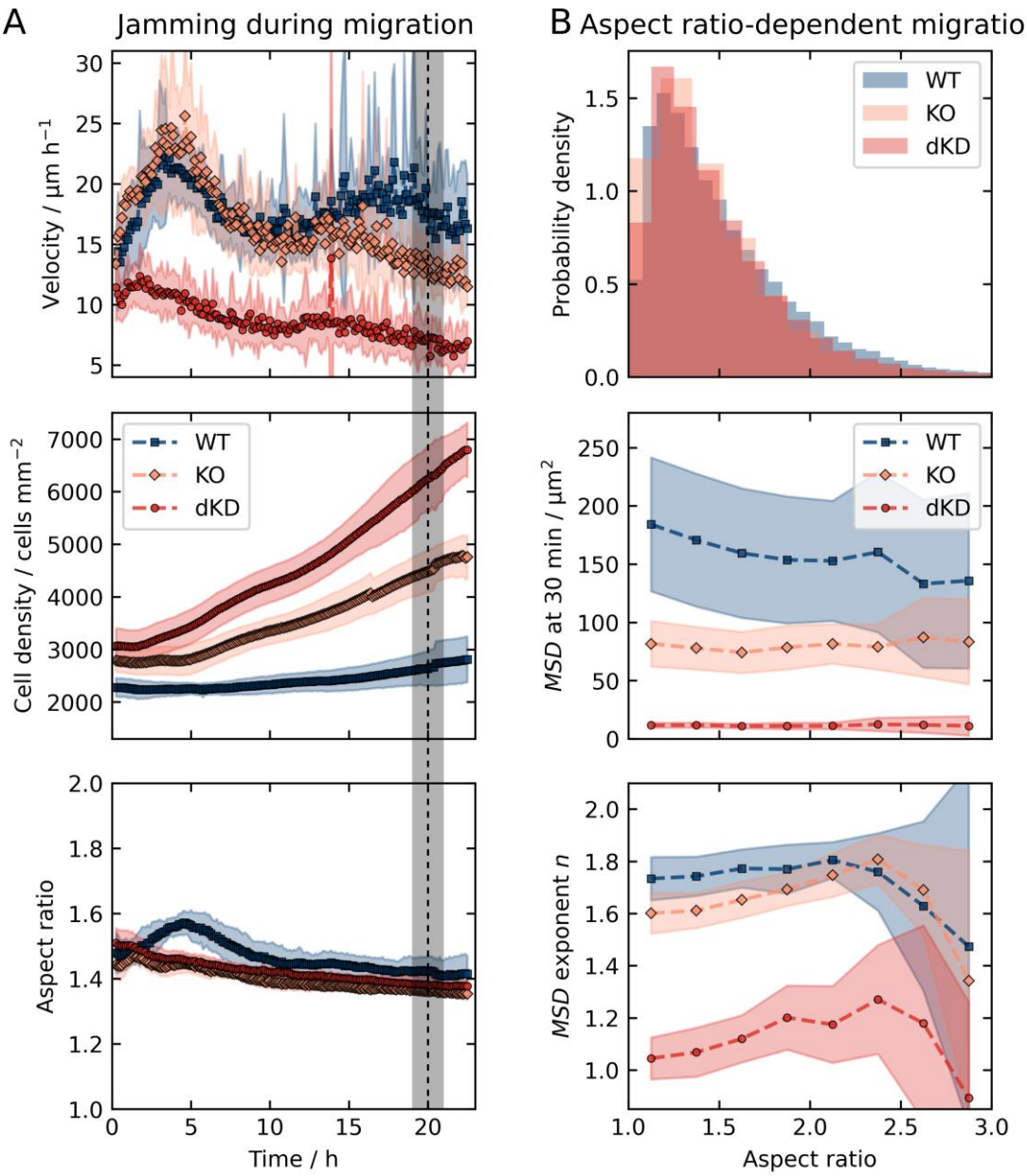

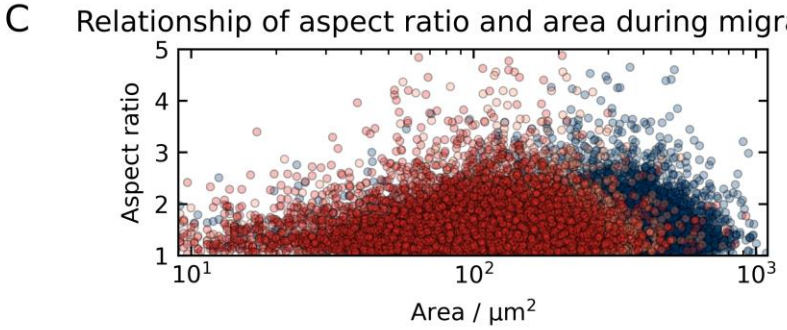

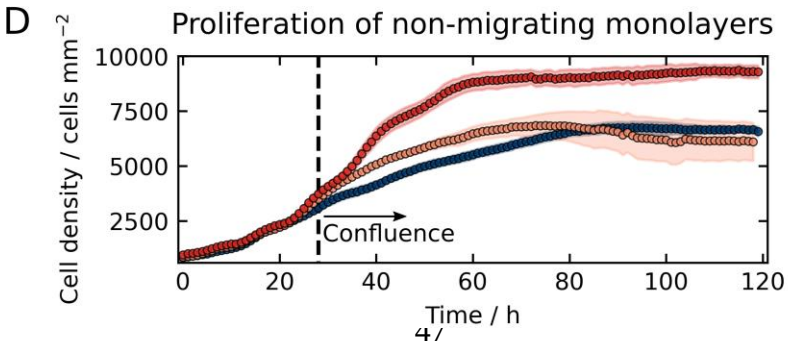

Figure S1. Temporal evolution of cell density, velocity, and aspect ratio as well as aspect ratio-dependent motility of all three untreated MDCK II cell lines. A) Cell crowding and jamming during migration as quantified by the velocity, cell density, and aspect ratio over time. The gray shade at 19-21 h corresponds to the time window of the *MSD* analyses. B) Aspect ratio distribution and aspect ratio-dependent *MSD* parameters. C) The aspect ratio showed a high variance but no co-variation with the area. D) Additional proliferation experiment immediately after seeding of cells without insert. The dashed line indicates reaching of confluence at 28 h, corresponding to the beginning of our typical migration experiments (0 h in all other figures). Means and standard deviations are shown. The aspect ratio in A is the median for each experiment and then averaged over all experiments.

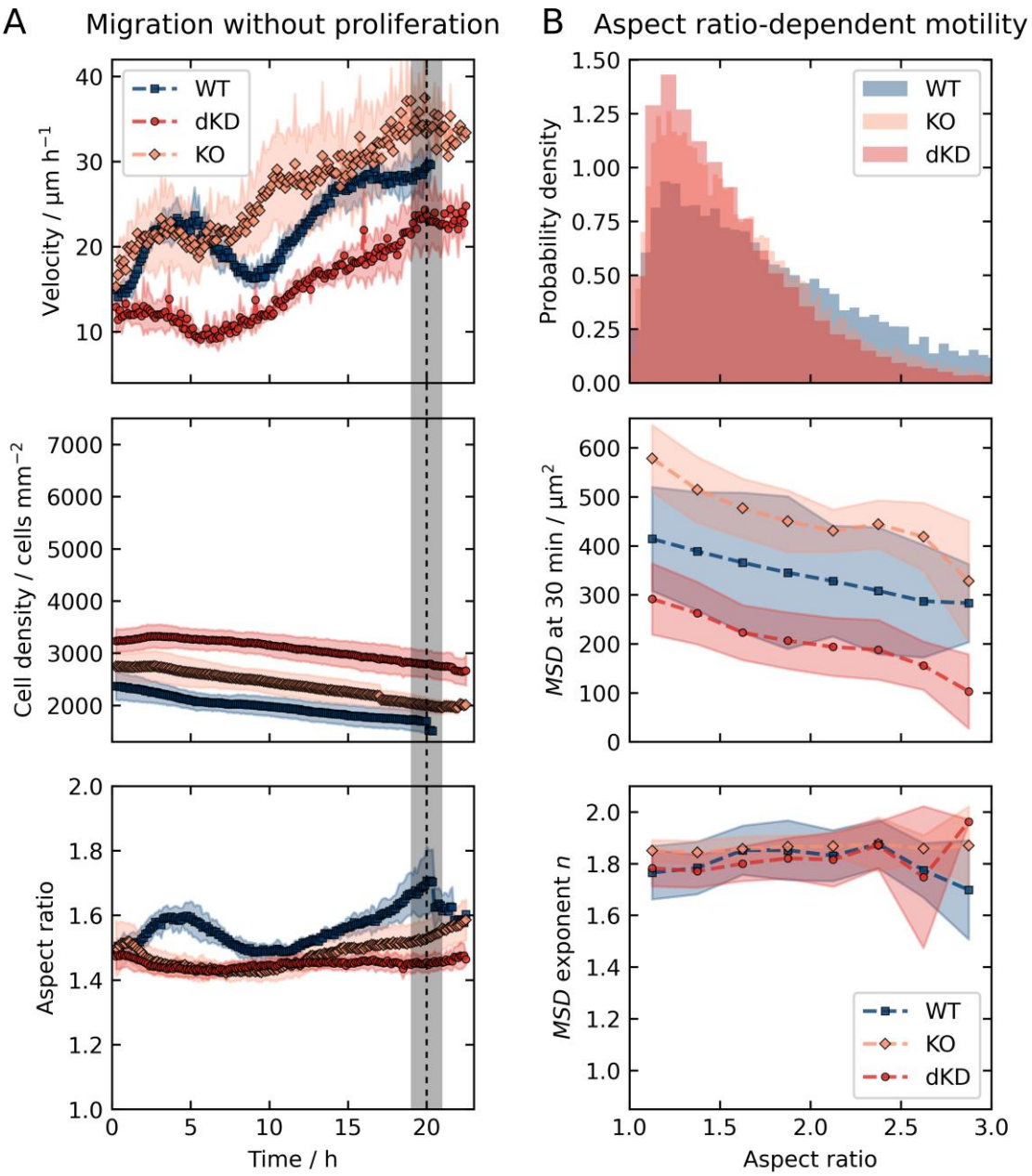

Figure S2. Temporal evolution of cell density, velocity, and aspect ratio as well as aspect ratio-dependent motility of all three MDCK II cell lines upon proliferation inhibition by Mitomycin C. A) Cell crowding and jamming were prevented by proliferation inhibiton during migration as quantified by the velocity, cell density, and aspect ratio over time. The gray shade at 19-21 h corresponds to the time window of the *MSD* analyses. B) Aspect ratio distribution and aspect ratio-dependent *MSD* parameters. Means and standard deviations are shown. The aspect ratio in A is the median for each experiment and then averaged over all experiments.

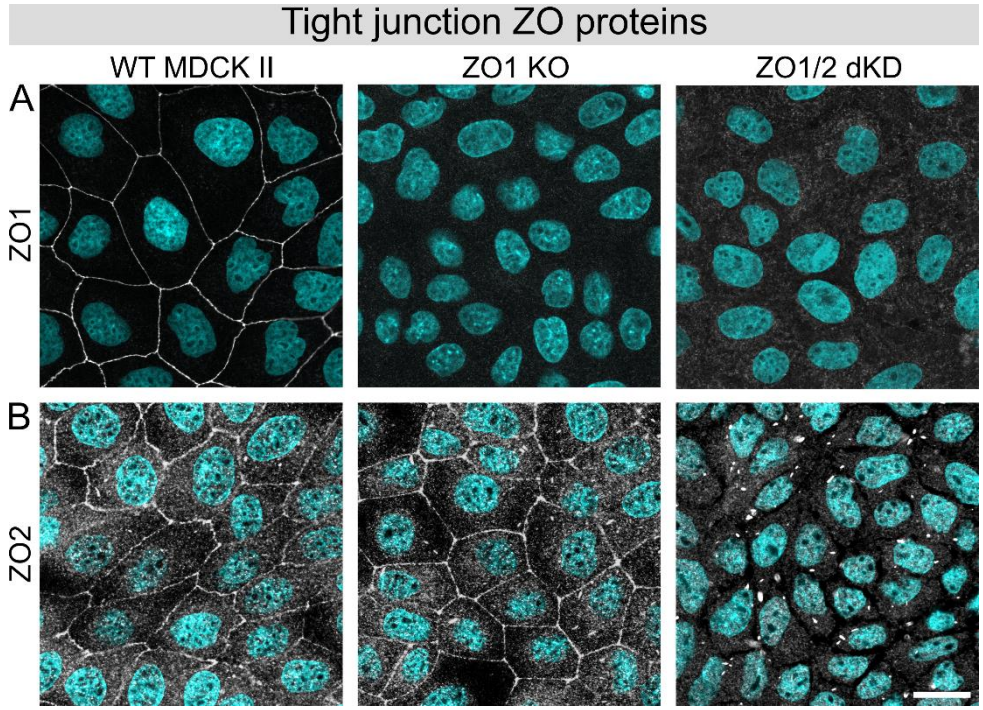

Figure S3. Immunofluorescence measurements confirming successful ZO protein knockout/-down. A) ZO1 antibody-based staining of all three MDCK II cell lines. B) ZO2 antibody-based staining of all three MDCK II lines. Nuclei are shown in cyan. Scale bar: 20 µm.

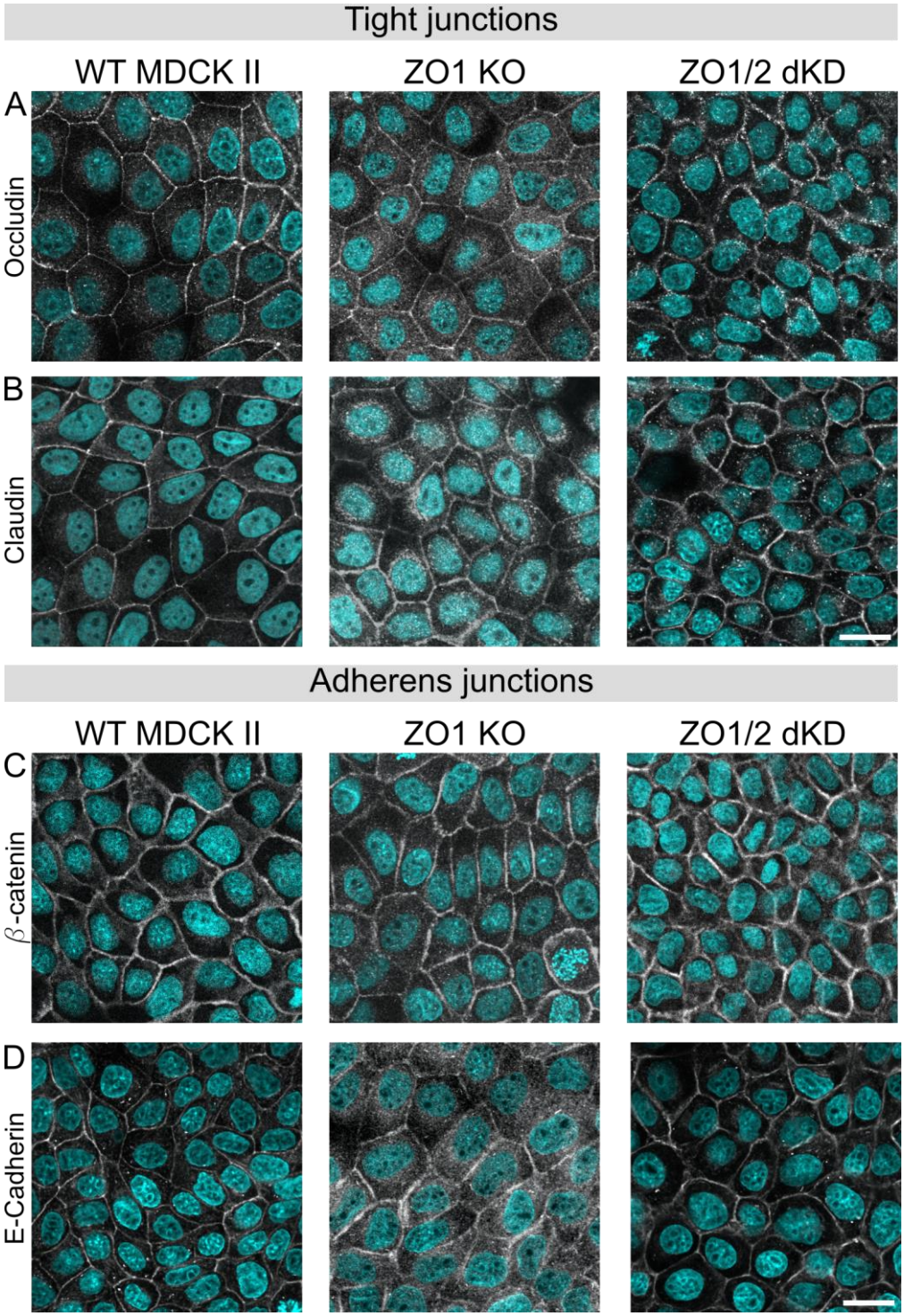

Figure S4. Immunofluorescence of tight junction transmembrane proteins and adherens junction proteins. A) Occludin. B) Claudin 1. C) β-catenin. D) E-Cadherin. Nuclei are shown in cyan. Scale bars: 20 µm.

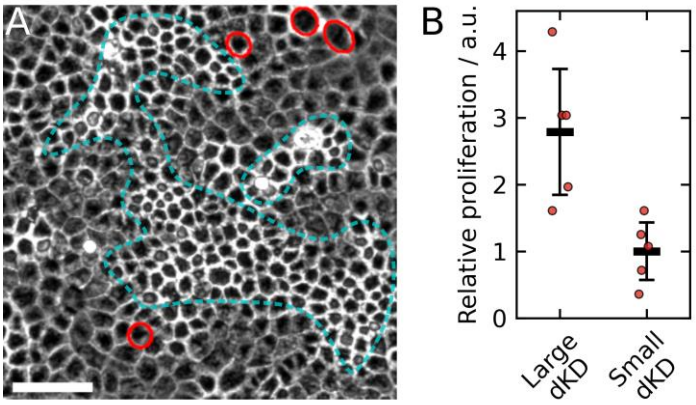

Figure S5. In the dKD monolayers, more of the large and stretched cells were observed to proliferate than the small and contractile cells. A) Example of dKD cells during migration with proliferation events indicated by red circles and patches of small cells highlighted in cyan. B) Relative proliferation of five example regions from A, normalized by the average number of small cell proliferation events. Proliferation events were counted and attributed by hand and the examples were chosen, so that approximately the same amount of large and small cells was present. These data were collected in the same time window as the MSD analysis, i.e., between 19 h and 21 h.